# Pasamonte

Polymict Eucrite, 3-4 kg

*Seen to fall*

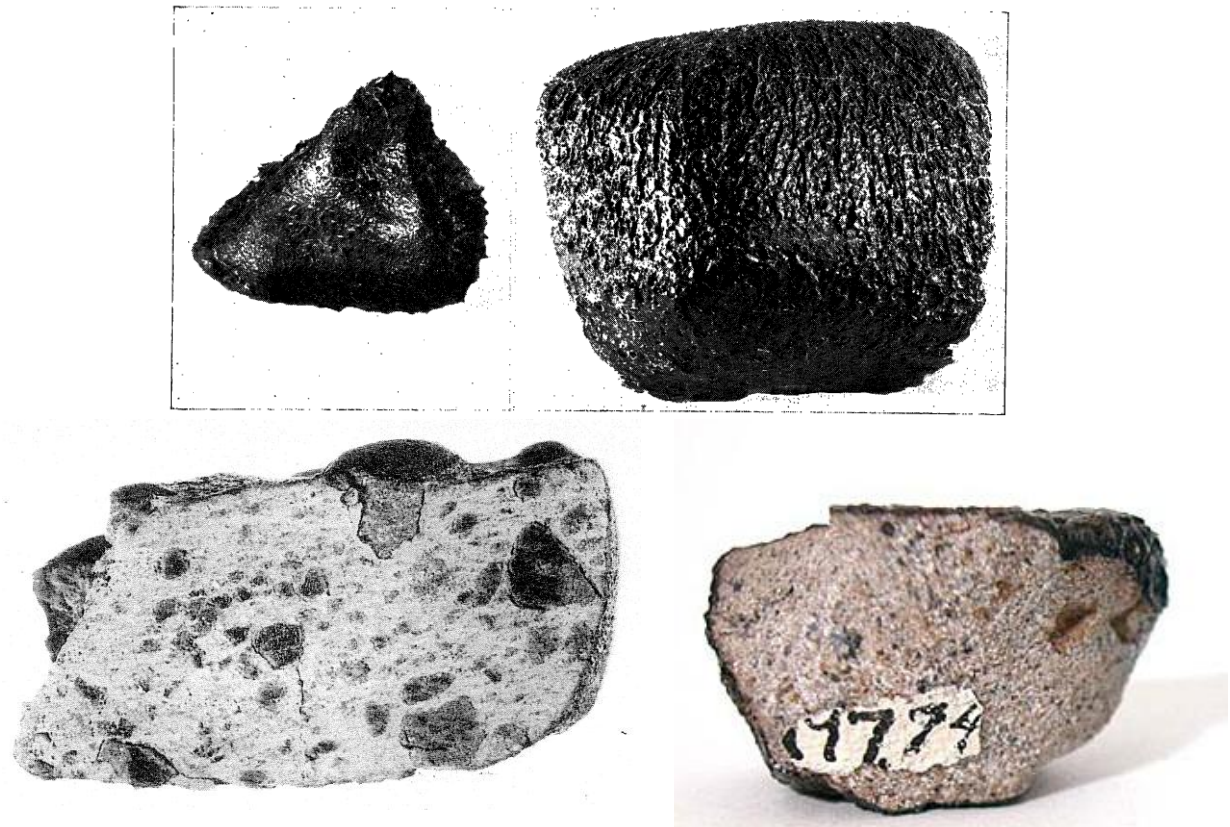

***Figure 1:*** *Photographs of different stones associated with the Pasamonte fall. The top image, from Nininger (1936), shows two stones with black, glassy fusion crusts; the left stone shows rear-pointing glass "teeth" at the junction of the sides with the base, but no prominent glass ridges, while the right stone exhibits strongly-defined ridges of glass. The bottom images (left: Watson, 1956; right: Martin Horejsi, Encyclopedia of Meteorites online) show the interior of the meteorite, with dark, large mineral and lithic clasts set in a light gray, fine-grained, comminuted matrix of similar materials.*

**Introduction:** The Pasamonte eucrite (**Figure 1**) fell at 5 AM on the morning of March 24$^{th}$, 1933, and was seen by numerous individuals in Kansas, Oklahoma, Texas, Colorado, and New Mexico before coming to rest near Pasamonte, New Mexico (Nininger, 1934; 1936; **Figures 2a, 2b**). The detonations associated with the meteorite could be felt and heard for one hundred miles on either side of its flight path, and the fall was seen by individuals up to three hundred miles away (Nininger, 1936). Varying witness reports indicated several bright fireballs followed by an extremely luminous "after-glow" and a lingering, 200-mile long dust cloud that was visible for up to 90 minutes after the meteor had passed (Nininger, 1934; **Figure 3**). Seventy-five stones were collected in the two years following the fall, with a

total weight of 3-4 kg (Foshag, 1938); the largest stone weighed less than 300 grams (Nininger, 1936). The largest weight fractions of the Pasamonte stones can be found at the Smithsonian National Museum

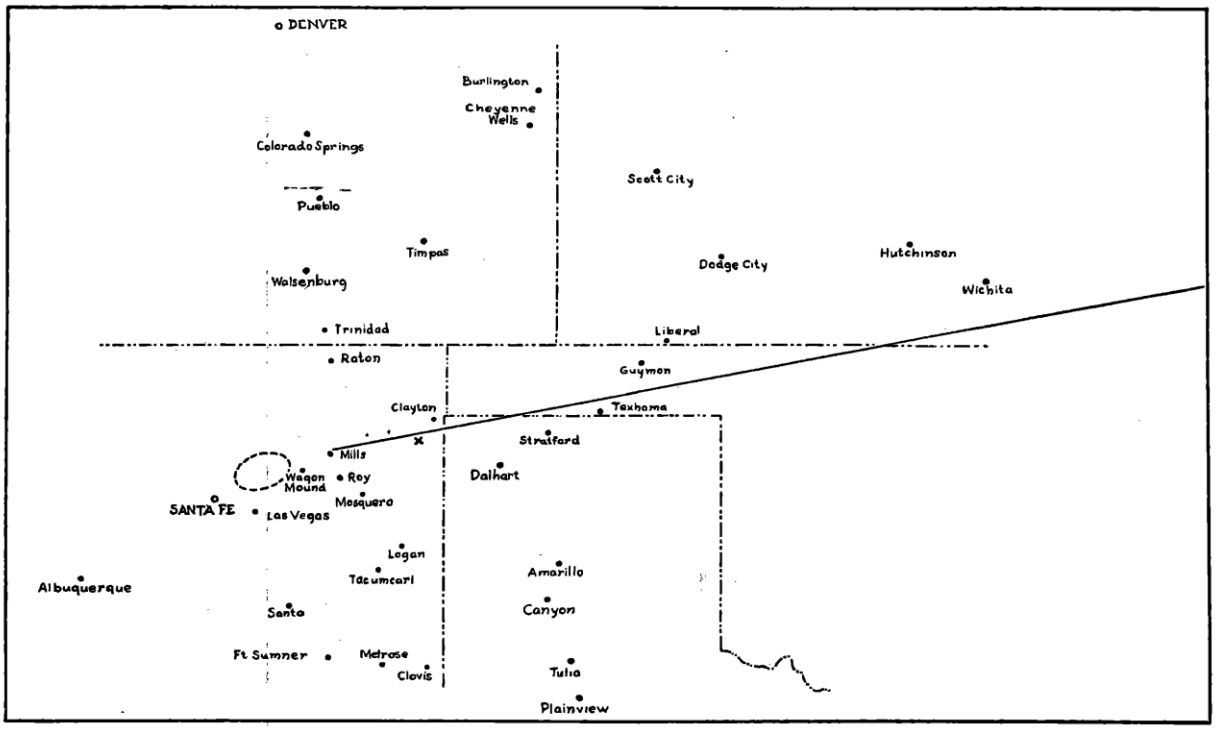


***Figure 2a**: Map of the Pasamonte flight path, based on numerous witness testimonies from surrounding towns marked on the map. The "X" along the flight path marks the location from which the top left photograph in **Figure 3** was taken. This map was made prior to any actual meteorite collection, but the two dots between Mills and Clayton marked the location of preliminary meteorite fragments. From Nininger (1934), no scale given.*

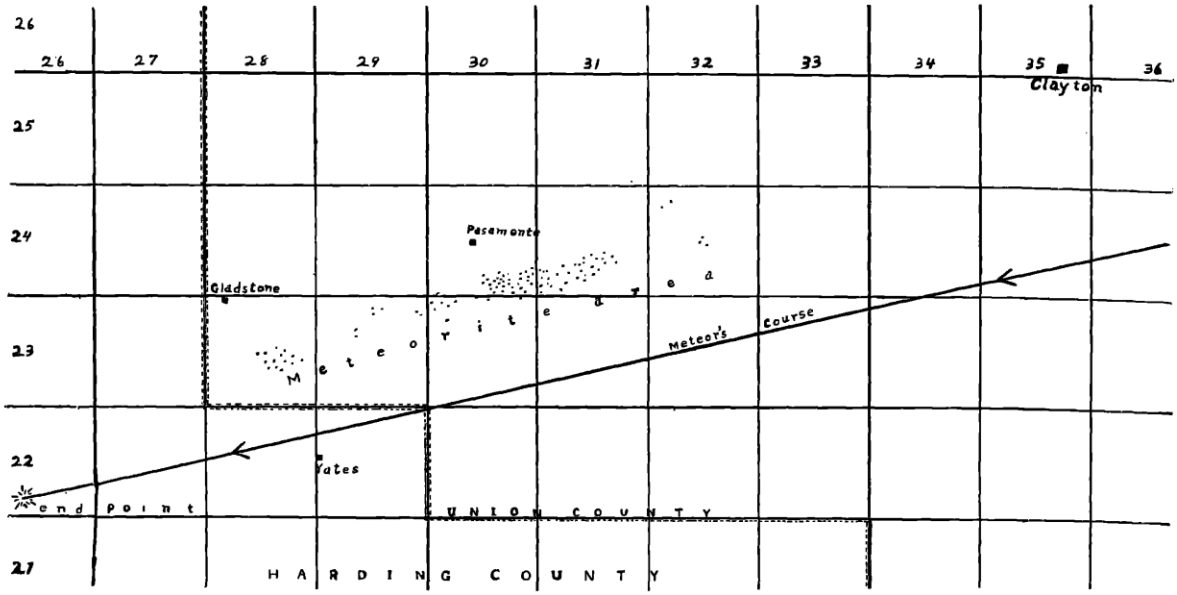


***Figure 2b**: Township map of Union County, New Mexico, with the plotted meteor's course (derived from witness testimony) and the location of the meteorite collection area. These stones were found between four and five miles north of the course of the meteorite, but in a roughly parallel arrangement, due to a strong wind blowing from the south; the largest stones were found to the southeast. From Nininger (1936).*

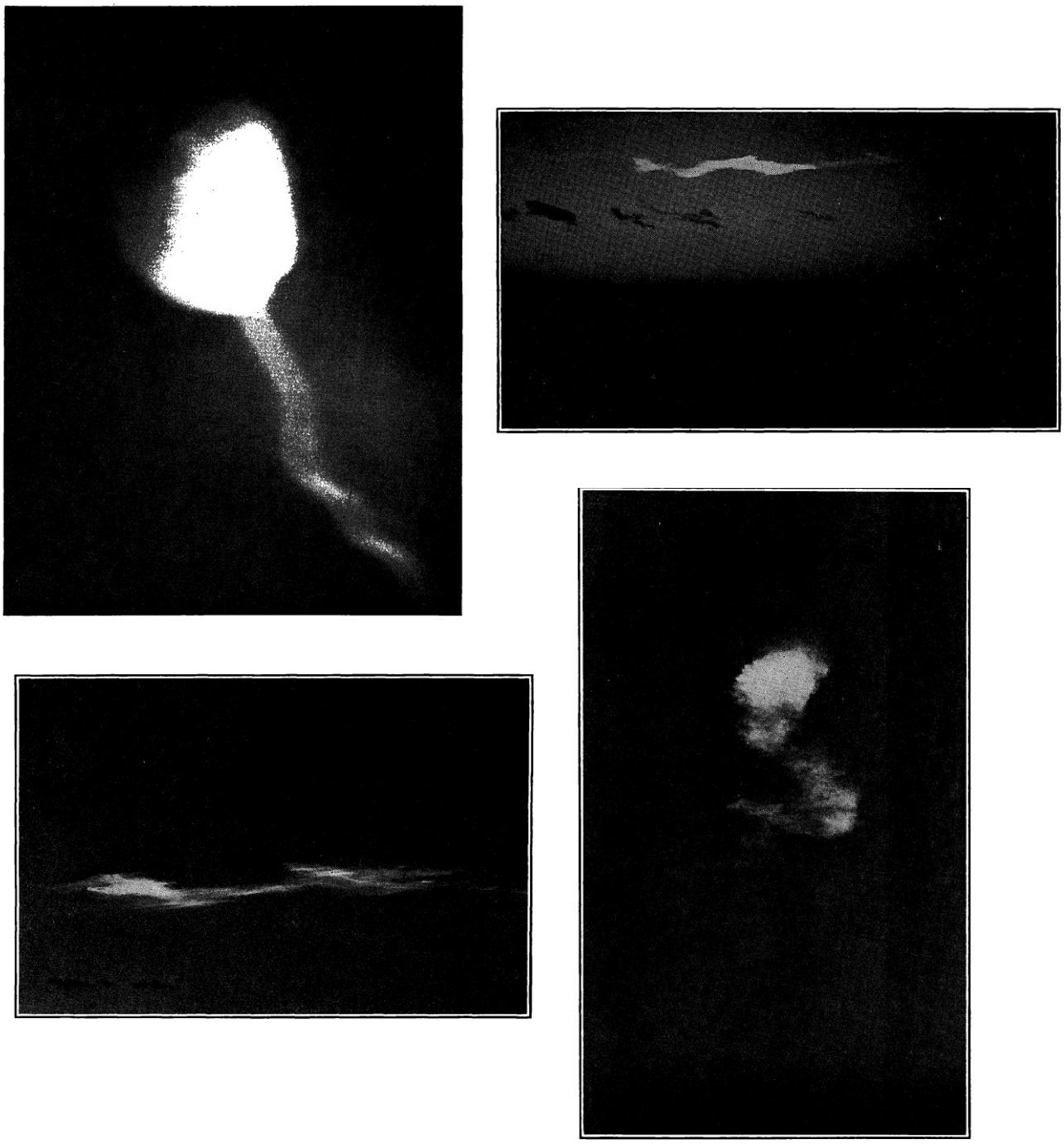

***Figure 3****: Witness photographs of the Pasamonte meteorite fall. The top left photograph shows the meteorite in flight, while the other three show the luminous "after-glow" remaining after the meteorite had passed. All photos published in Nininger (1934). Photo credits, clockwise from top left: Mr. Chas M. Brown; C.R. West; Bert D. Latham; C.R. West.*

in Washington, D.C. (1.29 kg), Arizona State University in Tempe (680 g), and the University of New Mexico in Albuquerque (221 g) (Grady, 2000).

Pasamonte stones have a black, heavy fusion crust, with prominent glass ridges, polygonal cooling cracks, fusion bubbles, and minor pitting (Nininger, 1936; Foshag, 1938). Approximately 50% of the

stones show a definite orientation, with the rear face exhibiting a "tar-like" glaze containing gas bubbles and explosion pits, and the front face showing either prominent ridges or none at all (Nininger, 1936). Those stones that were non-oriented, however, show strong glass ridges (Nininger, 1936). Some fragments show a dull, reddish color that may be evidence of surficial weathering (Foshag, 1938).

Pasamonte is a brecciated, polymict eucrite; it was initially classified as a eucritic breccia, i.e., a howardite (Foshag, 1938) or a monomict eucrite (Duke and Silver, 1967; Takeda et al, 1976a) before being reclassified as a polymict eucrite based on mineral and lithic clasts that showed markedly different major, minor, and trace element chemistries (Metzler et al 1994; 1995). However, these clasts are all eucritic; no diogenitic clasts have been found (Metzler et al, 1995), and thus Pasamonte is *not* a howardite. Many pyroxene fragments in Pasamonte show one of four types of zoning (Takeda et al, 1976a; Takeda et al, 1978a; Miyamoto et al, 1985; Schwartz and McCallum, 2005), and there is plagioclase zoning as well (Duke and Silver, 1967; O'Neill and Delaney, 1982; Batchelor, 1991; Hsu and Crozaz, 1996), though not all crystals of either mineral are zoned (Metzler et al, 1994; Metzler et al, 1995; Hsu and Crozaz, 1996). These and other features indicate that Pasamonte experienced relatively weak metamorphism on its parent body, and it is thus classified as a rare Type 2 eucrite on the metamorphic scale of Takeda and Graham (1991).

**General Petrography**: The unique circumstances of the Pasamonte meteorite fall were described in detail in Nininger (1934, 1936); some general petrologic observations were made by Nininger (1936), but the first detailed petrographic analyses were reported by Foshag (1938).

Pasamonte is a brecciated, non-cumulate, polymict eucrite, showing dark fine- to medium-grained, subhedral to euhedral, lithic and mineral fragments set in a light, friable, sugary, ash-gray matrix with a high porosity (Foshag, 1938; Unruh et al, 1977; Metzler et al, 1995; Hsu and Crozaz, 1996). Rock fragments show a range of textures, including classic ophitic (**Figure 4**), subophitic (**Figure 5**), granulitic, and brecciated granulitic (**Figure 6**) varieties (Foshag, 1938; Duke and Silver, 1967; Takeda et al, 1976a; Takeda et al, 1978a; BVSP, 1981; Metzler et al, 1994; Metzler et al, 1995; Schwartz and McCallum, 2005), the last of which shows evidence for projectile contamination (Metzler et al, 1995; **Figure 7**). Some authors have reported abundant fine-grained plumose, acicular, and sheaf-like pyroxenes intergrown with plagioclase (Foshag, 1938; Miyamoto et al, 1985); these are probably the same as variolitic or "fan-spherulitic" clasts described by other authors (e.g., BVSP, 1981; Metzler et al, 1994; Metzler et al, 1995; Schwartz and McCallum, 2005; **Figure 8**). Unusual fragments are present as well, including dark, heavy, opaque "slag-like" fragments with irregular shapes (Foshag, 1938), which may be related to the dark, fine-grained impact melt breccias described by Metzler et al (1994, 1995). Similar glassy clasts have also been reported in the literature, with major and trace element chemistries that mirror those of the bulk Pasamonte composition, and thus were probably formed by impact melting processes (Phinney et al, 1993; Hsu and Crozaz, 1996). Finally, Schwartz and McCallum (2005) reported symplectitic clasts that were inferred to represent decomposition from forbidden-zone pyroxene compositions. The lithic clasts described above can occur in unequilibrated or equilibrated varieties (Metzler et al, 1994; 1995).

Mineral fragments show glassy, white, yellow, and brown varieties (Foshag, 1938), and are mostly pigeonite with accessory plagioclase (Mason et al, 1977; Schwartz and McCallum, 2005). The main constituent minerals, in both lithic and mineral fragments, are up to 2-mm sized, mostly unclouded pyroxenes and ≤6 mm clouded plagioclase (Foshag, 1938; Harlow and Klimentidis, 1980; Schwartz and McCallum, 2005), with accessory tridymite, mesostasis, chromite, ilmenite, troilite, phosphates, and Fe-Ni metal. Mineral fragments of pyroxene and plagioclase can occur in unequilibrated *or* equilibrated

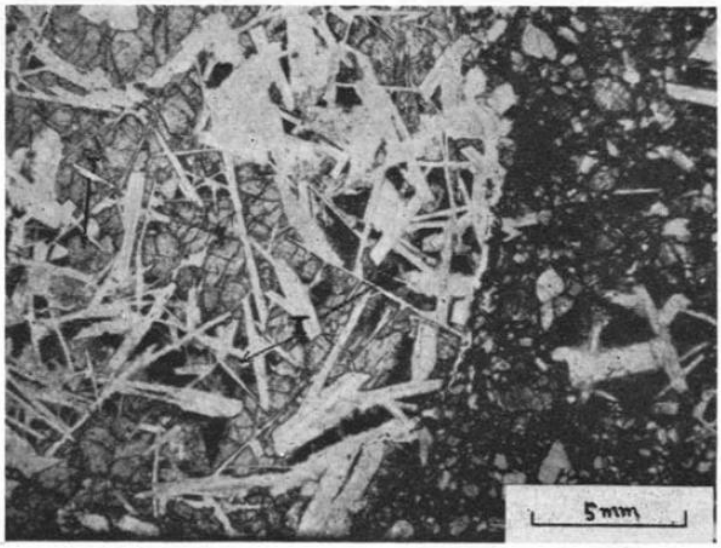


***Figure 4**: Plane polarized light photomicrograph of Pasamonte, showing a fragment with ophitic texture (left) embedded in a fine-grained matrix (right). Pyroxenes in this fragment are strongly zoned, with colorless Mg-rich cores and dark brown Fe-rich rims that also contain inclusions of troilite. From Duke and Silver (1967). Scale bar in lower right corner is 5 mm.*

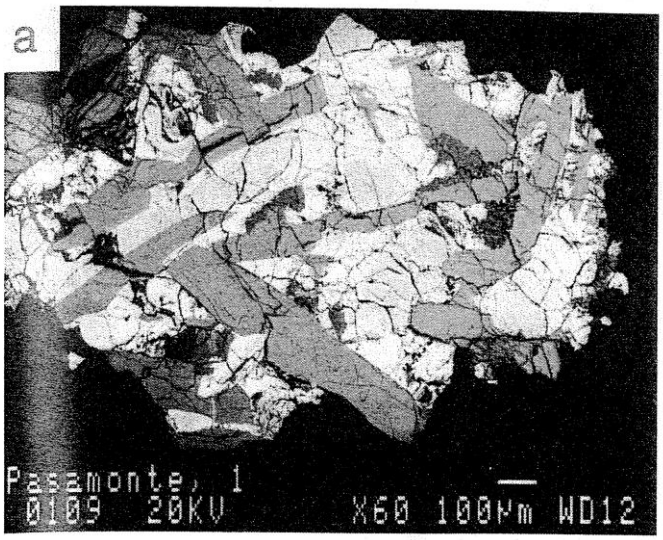


***Figure 5**: BSE image of a subophitic basalt clast from Pasamonte. From Metzler et al (1995); the white scale bar in the lower right corner is 100 µm.*

***Figure 6**: BSE image of a granulite breccia clast from Pasamonte. From Metzler et al (1995); the white scale bar in the lower right corner is 100 µm.*

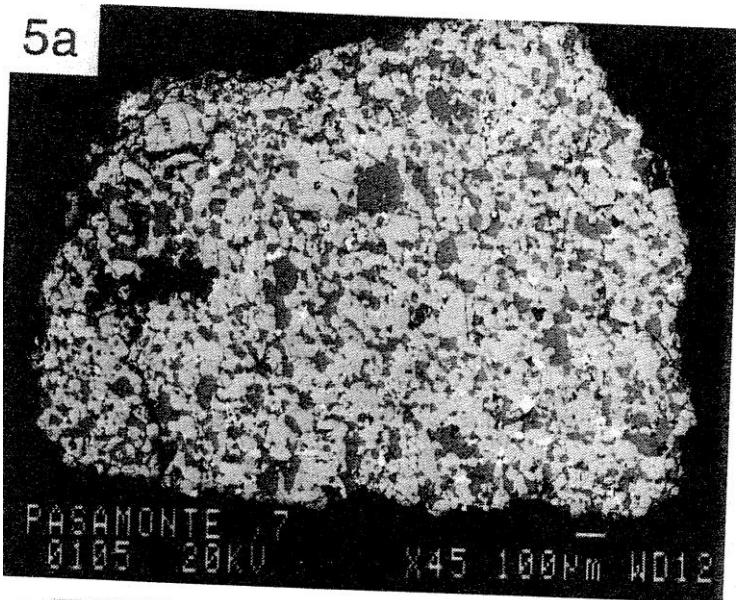

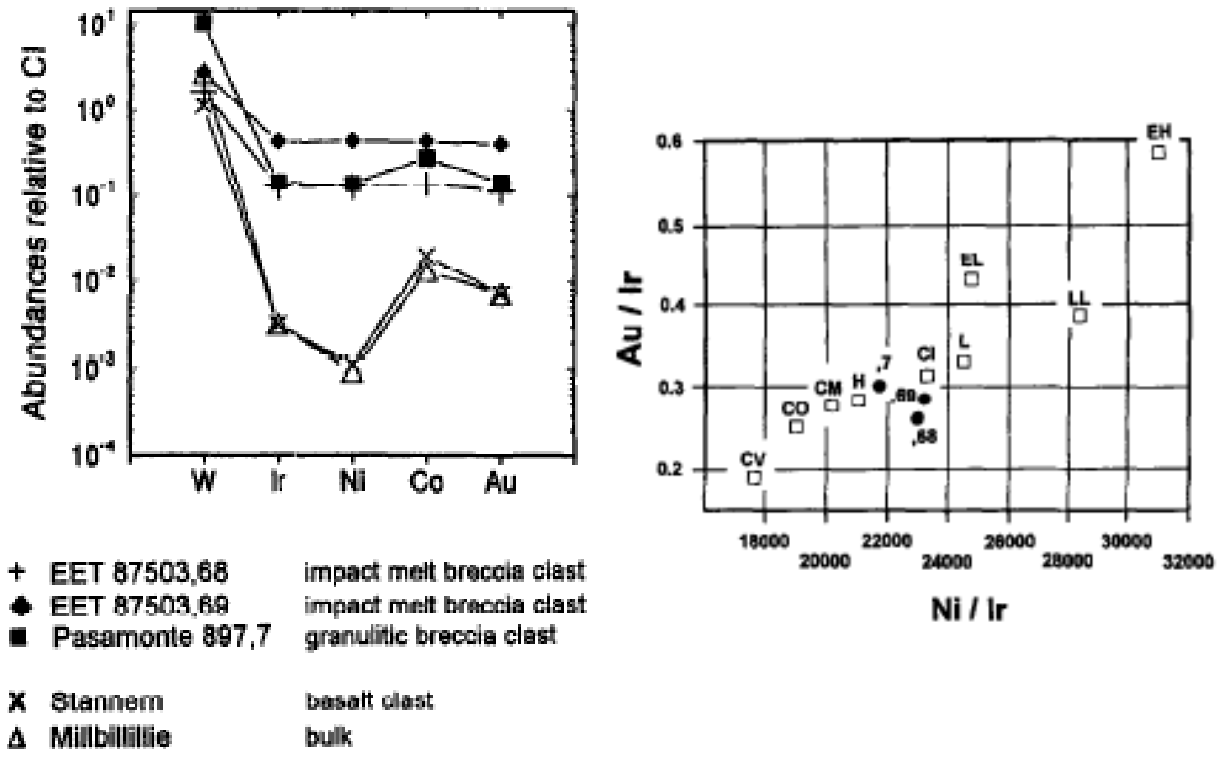


***Figure 7**: Siderophile element concentrations (left) in the granulite breccia clast from Pasamonte (filled squares; see **Figure 6** for a BSE image of the clast), impact melt clasts from an Antarctic howardite, and "normal" eucrites (Stannern and Millbillillie). The Pasamonte clast shows relatively flat enrichment in these elements as compared to the normal eucrites, with an especially high W abundance (probably related to the presence of metal within this clast). Au/Ir and Ni/Ir ratios for this clast (right, filled circle marked ",7") plot between H and CI chondrites, suggesting that Pasamonte was at some point contaminated with chondritic material from an H or CI source. Both diagrams from Metzler et al (1995).*

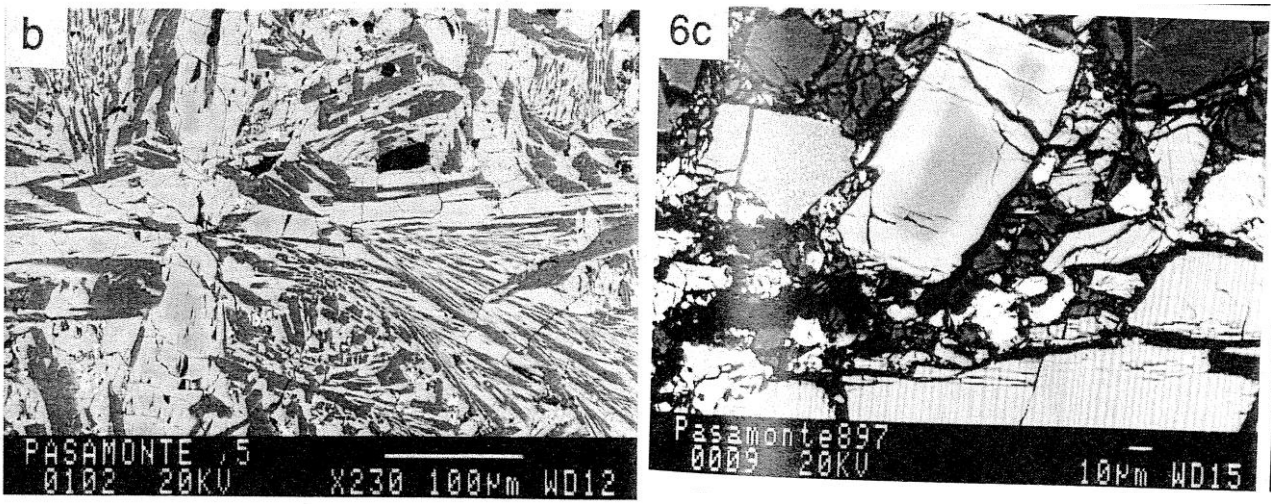


***Figure 8 (left)**: BSE image of a variolitic basalt clast from Pasamonte. From Metzler et al (1995).*

***Figure 9 (right)**: An unequilibrated pyroxene clast (top, center) next to an equilibrated clast with obvious exsolution lamellae (bottom, right). From Metzler et al (1995).*

(i.e., zoned and unzoned) varieties; equilibrated pyroxenes are usually larger, with ≤5 µm exsolution la mellae, while unequilibrated pyroxenes show only submicroscopic (i.e., not optically visible) exsolution lamellae (Takeda et al, 1976a; Metzler et al, 1994; Metzler et al, 1995; Hsu and Crozaz, 1996). There have also been a few reports of rare olivine, as well as zircon-bearing minerals (Miyamoto et al, 1985; Bukovanska and Ireland, 1993; Schwartz and McCallum, 2005); these are discussed below in the section covering mineral petrography and chemistry. Normative and modal mineralogy is shown in **Table 1**.

Nininger (1936) remarked that Pasamonte consisted of a "tufaceous material, much of which is so finely divided that, when a piece of the stone is broken or rubbed, it emits a cloud of dust so fine that it rises like smoke from a cigarette." He inferred that the unusually large dust cloud seen after the passing the meteorite was derived from sections of this fine-grained material that escaped volatilization and liquefaction (Nininger, 1936). A microscopic analysis of the Pasamonte groundmass showed angular fragments of plagioclase, pigeonite, and other crushed eucritic fragments (Foshag, 1938; Miyamoto et al, 1985).

**Table 1**: Normative and modal mineralogy of Pasamonte.

| **reference** | **Foshag 38** | **Duke and Silver 67** | | **Bunch 75** | **Prinz et al 80** | **BVSP 81** | **Delaney et al 84e** | **Kitts and Lodders 98** | |
|---|---|---|---|---|---|---|---|---|---|
| type | norm | mode | norm | norm | mode | norm | mode | norm (wt %) | norm (vol %) |
| comments | -- | -- | -- | basalt clast | impact melt | | -- | -- | -- |
| pyroxene | 63 | 63 | 59.1 | 52.47 | 49.7 | 58.92 | 50.7 | 57.7 | 52.2 |
| plagioclase | 29.5 | 30 | 36.3 | 38.69 | 40.8 | 35.58 | 41.9 | 36.2 | 42.4 |
| tridymite | 3 | 3 | 2 | 7.41 | 8.9 | 1.9 | 5 | 3.3 | 4 |
| ilmenite | -- | -- | -- | 1.47 | 0.4 | 1.37 | 1.2 | 1.4 | 0.9 |
| chromite | 1.5 | -- | -- | -- | 0.1 | 0.46 | 0.1 | 0.4 | 0.3 |
| troilite | -- | -- | -- | -- | -- | -- | 1.1 | -- | -- |
| phosphates | -- | -- | -- | -- | 0.1 | 0.24 | 0.1 | 0.2 | 0.2 |
| metal | 2.5 | -- | -- | -- | -- | -- | 0.1 | -- | -- |

**Mineral Petrography and Chemistry**

*Pyroxene.* The main pyroxene in Pasamonte was identified as pigeonite by Foshag (1938), who also noted that some grains appeared to show a chemical gradation corresponding to a color change from very light brown to dark gray-brown. This color change was also discussed by Duke and Silver (1967), with the lighter pyroxene compositions reflecting Mg-rich pigeonite cores, and the dark brown pyroxenes reflective of Fe-rich compositions at the pigeonite rims, which also contain abundant troilite inclusions (e.g., **Figure 4**). Small (~100 µm) single grains of dark brown, Fe-rich or subcalcic ferroaugite and ferropigeonite ($Ca_{30-40}Mg_{20-28}Fe_{40-54}$) have been reported as late-forming minerals, as they are confined to pigeonite rims or the matrix (Duke and Silver, 1967; Takeda et al, 1976a, 1976b; Schwartz and McCallum, 2005).

The gradation from Mg-rich to Fe-rich pyroxene was taken as clear evidence of preserved igneous zoning, and thus the unequilibrated nature of Pasamonte, as equilibrated pyroxenes have had chemical zoning obliterated by intracrystalline diffusion (Duke and Silver, 1967; Reid and Barnard, 1979; Delaney et al, 1982a). However, it is important to note that there are lithic clasts that are clearly equilibrated

with no evidence of pyroxene zoning (**Figure 9**), implying a polymict origin for Pasamonte, and thus the term "Pasamonte-type" (as applied to pyroxenes from other eucrites) should be avoided (Metzler et al, 1994, 1995; Hsu and Crozaz, 1996).

Pasamonte was initially reported as lacking metastable, Fe-rich pyroxenes that plot inside the forbidden zone of pyroxene stability; as these are present in some unequilibrated Antarctic eucrites (e.g., Y-75011), it was interpreted that some equilibration took place even on the most unequilibrated Pasamonte pyroxenes (Takeda et al, 1983). However, later authors have found examples of Fe-rich pyroxenes within the forbidden zone, including those of the fourth zoning type (described below) (Schwartz and McCallum, 2005), and there is also abundant evidence of decomposition from these pyroxenes to Fe-metal, Fe-rich orthopyroxene, Fe-rich olivine, augite, and silica (Hsu and Crozaz, 1996; Schwartz and McCallum, 2005), especially in irregular patches *within* preserved metastable grains and in symplectitic clasts in the matrix (Schwartz and McCallum, 2005).

Major element zoning in unequilibrated Pasamonte pyroxenes can be defined as one of four types, with overall pyroxene compositions plotted in **Figure 10**. Each published study contains some variability in pyroxene compositions due to variability in pyroxene chemistry between different clasts (Metzler et al 1994, 1995; **Figure 11**) and two-dimensional cuts of broadly zoned pyroxenes (Miyamoto et al, 1985). There is also some variety in zoning classification, with many authors only reporting a subset of the four zoning types; I have chosen to use Miyamoto et al (1985) and Schwartz and McCallum (2005) as the basis for classification here.

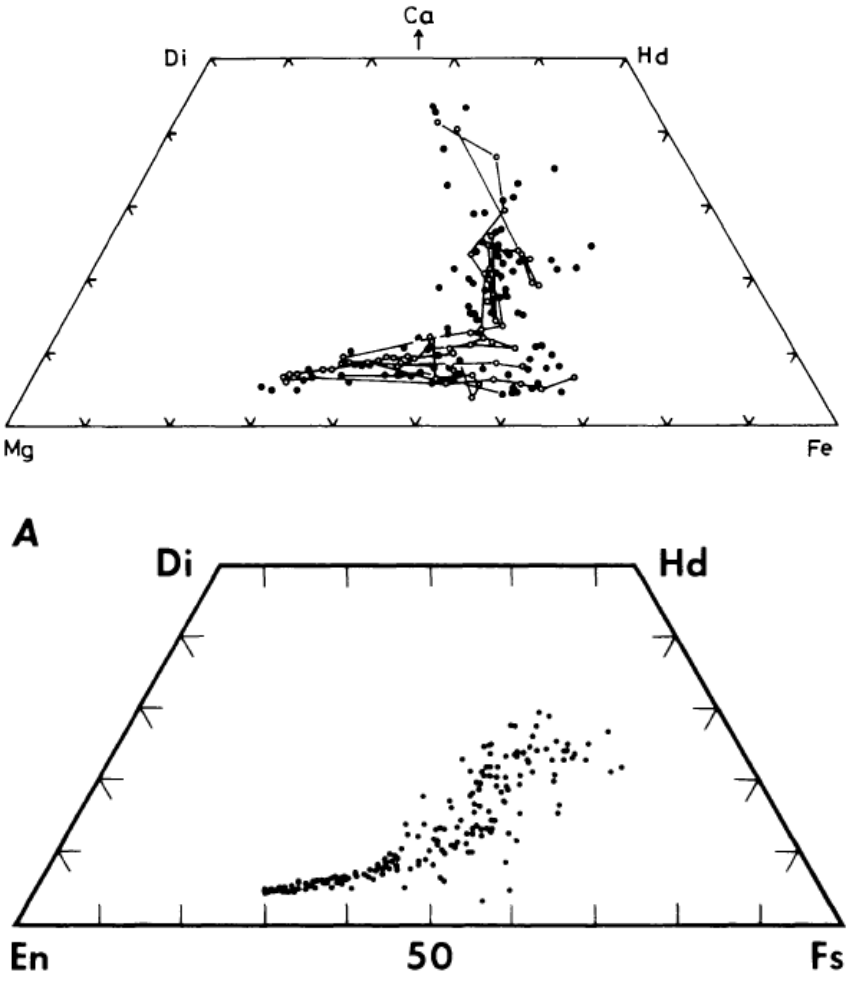


***Figure 10**: Measured pyroxene compositions in Pasamonte, with zoned compositions from the same crystals shown connected by tie lines (top diagram only). Top: Takeda et al (1976a), bottom: BVSP (1981).*

(1) Light yellow-brown Mg-rich pigeonite cores (~$Ca_5Mg_{62}Fe_{32}$) that show a gradational transition to darker Fe- and Ca-rich pigeonite and augite (~$Ca_{41}Mg_{20}Fe_{40}$), typical of pyroxene traverses that terminate in a mesostasis (Takeda et al, 1976a, 1978a; Miyamoto et al, 1985; **Figure 12**). Zoning Type 1 is likely a preserved, primary igneous texture (Miyamoto et al, 1985; Schwartz and McCallum, 2005).

(2) Light yellow-brown Mg-rich pigeonite cores (~$Ca_5Mg_{62}Fe_{32}$) that show a gradational transition to darker Fe- and Ca-enriched pigeonite or augite (~$Ca_{25}Mg_{34}Fe_{41}$), but are generally less Fe- and Ca-enriched than Type 1 (Miyamoto et al, 1985; **Figure 13**). This zoning is typical for pyroxenes that terminate at plagioclase crystals (Takeda et al, 1978a; Miyamoto et al, 1985), as the plagioclase grains shielded the pyroxenes from the latest Fe- and Ca-rich melt (Delaney et al, 1982a; Miyamoto et al, 1985). Thus, it is likely a preserved, primary igneous feature (Schwartz and McCallum, 2005).

(3) Light yellow-brown Mg-rich pigeonite cores (~$Ca_5Mg_{62}Fe_{32}$) with darker Fe-rich pigeonite rims (~$Ca_7Mg_{32}Fe_{61+}$), showing a sharp boundary between core and rim (Takeda et al, 1976a; Miyamoto et al, 1985; Hsu and Crozaz, 1996; **Figure 14**). This is typical of pyroxenes in the matrix (Miyamoto et al, 1985). Zoning Type 3 is especially prominent adjacent to fractures within pyroxene grains, with pronounced diffusional textures that intersect coherent Cr lamellae (**Figure 14**); it is interpreted to represent partial equilibration through post-crystallization cryptic metasomatism by a dry, Fe-rich vapor (Schwartz and McCallum, 2005).

(4) Ferroaugite or ferropigeonite grains that show reverse-zoning at a nearly constant CaO content, with Fe-rich cores and Mg-enrichment at grain rims (Schwartz and McCallum, 2005; **Figure 15**). Like Type 3, Type 4 zoning is interpreted to represent partial equilibration through post-crystallization cryptic metasomatism by a dry, Fe-rich vapor (Schwartz and McCallum, 2005).

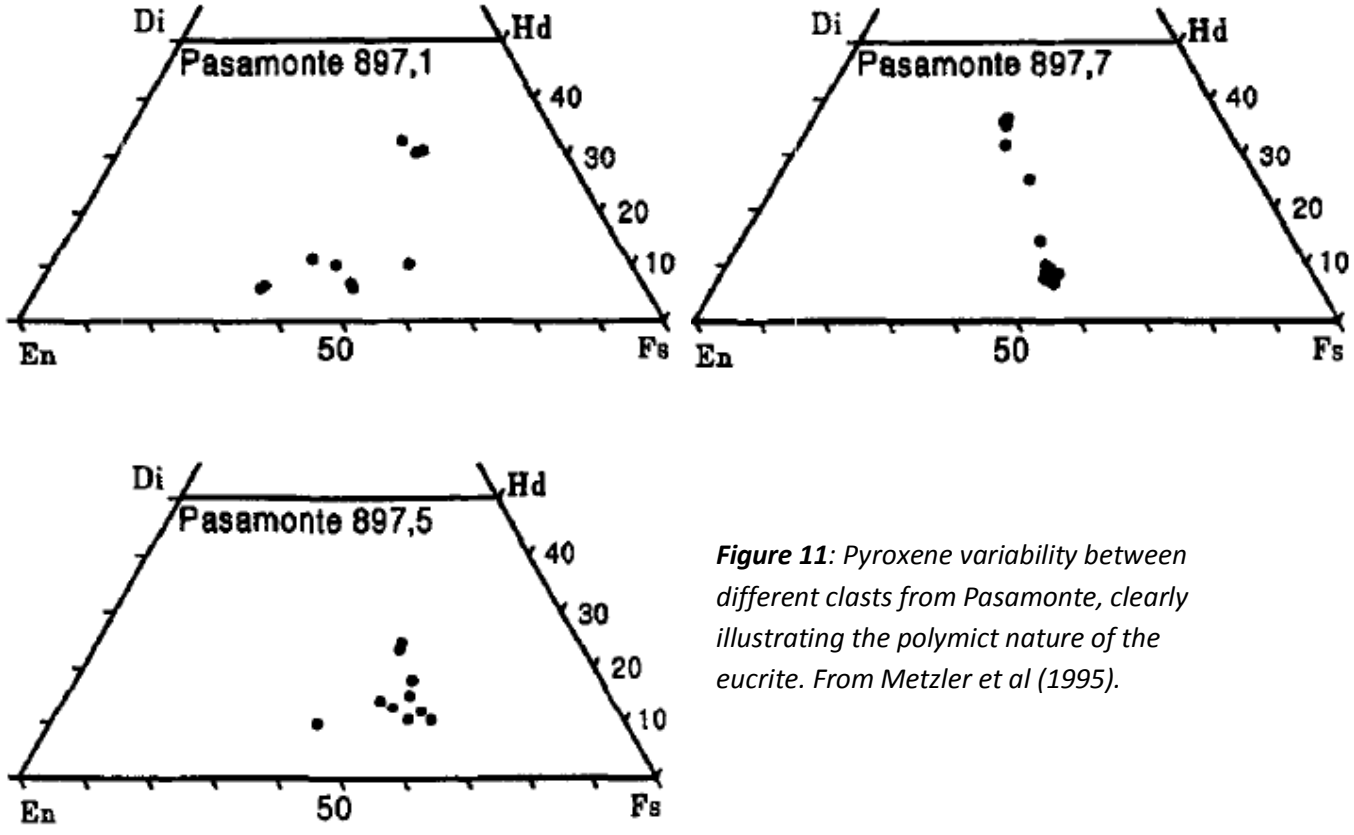


***Figure 11**: Pyroxene variability between different clasts from Pasamonte, clearly illustrating the polymict nature of the eucrite. From Metzler et al (1995).*

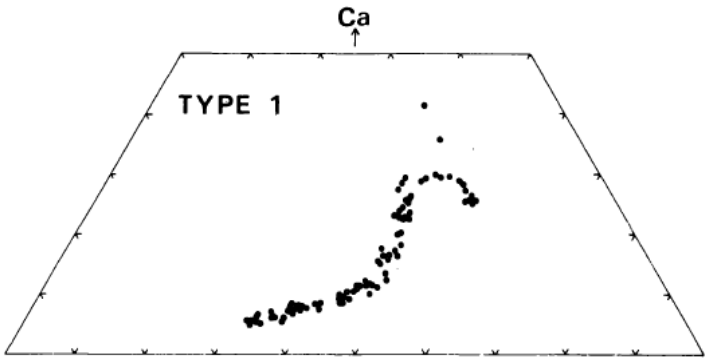


***Figure 12**: Type 1 zoning in Pasamonte pyroxenes, from Mg-rich cores to Fe- and Ca-rich rims. From Miyamoto et al (1985).*

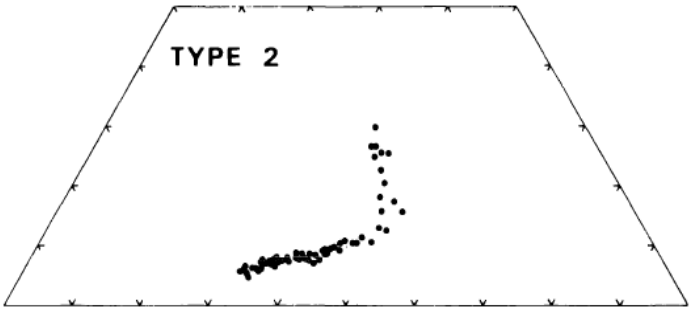


***Figure 13**: Type 2 zoning in Pasamonte pyroxenes, from Mg-rich cores to Fe- and Ca-rich rims; these pyroxenes are generally less enriched in both Fe and Ca than Type 1. From Miyamoto et al (1985).*

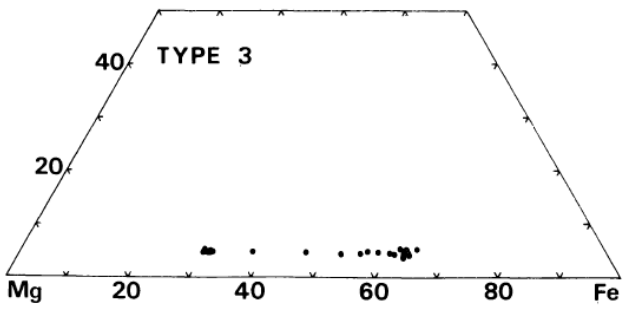


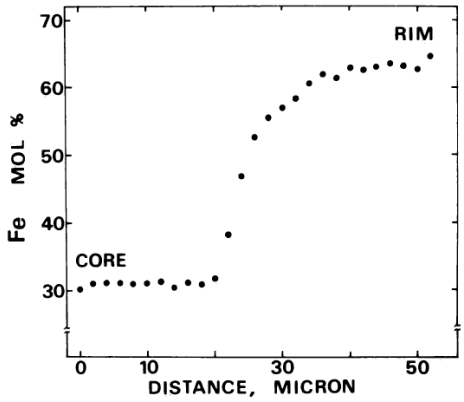


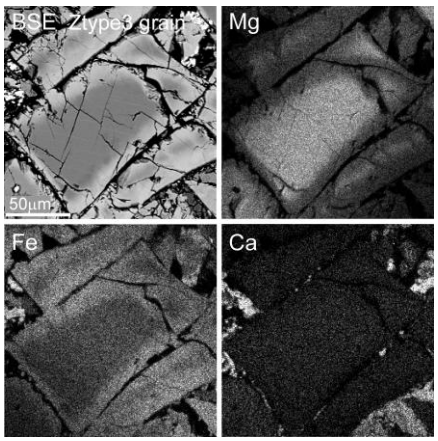


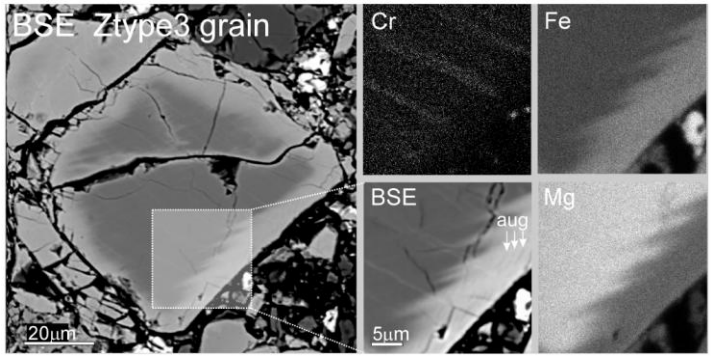


***Figure 14**: Type 3 zoning in Pasamonte pyroxene. The top two diagrams, from Miyamoto et al (1985), show sharp Fe-enrichment between the pyroxene cores and rims, with little change in Ca content. The bottom two figures, from Schwartz and McCallum (2005), show BSE and chemical zoning maps of pyroxenes with Type 3 zoning; Fe-enrichment is seen at both grain boundaries and interior fractures. Coherent Cr-lamellae are interrupted by an interdigitating texture in the bottom figure, indicating Fe-diffusion by late cryptic metasomatism.*

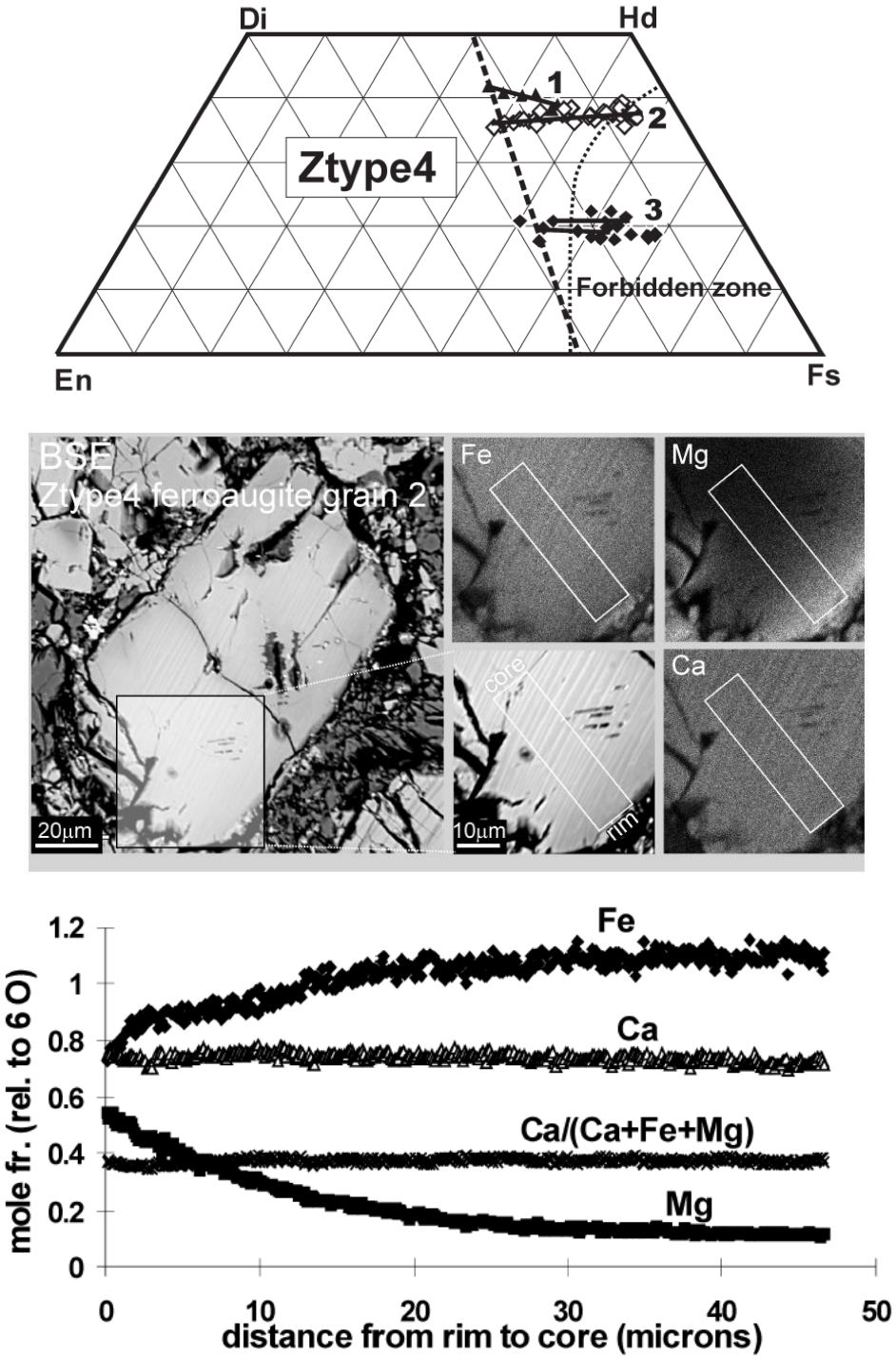


***Figure 15****: Type 4 zoning in Pasamonte pyroxenes (seen only in ferropigeonites and ferroaugites). Some compositions plot within the forbidden zone of pyroxene instability, and all show evidence of FeO metasomatism (top). The bottom two images reveal reverse zoning, with Fe decreasing and Mg increasing towards the rim of the grains (note the light, Mg-rich composition at the rim of the pyroxene in the compositional zoning map). This Mg-rich rim results from pyroxene reactions with the FeO-rich vapor accompanying metasomatism. All figures and images from Schwartz and McCallum (2005).*

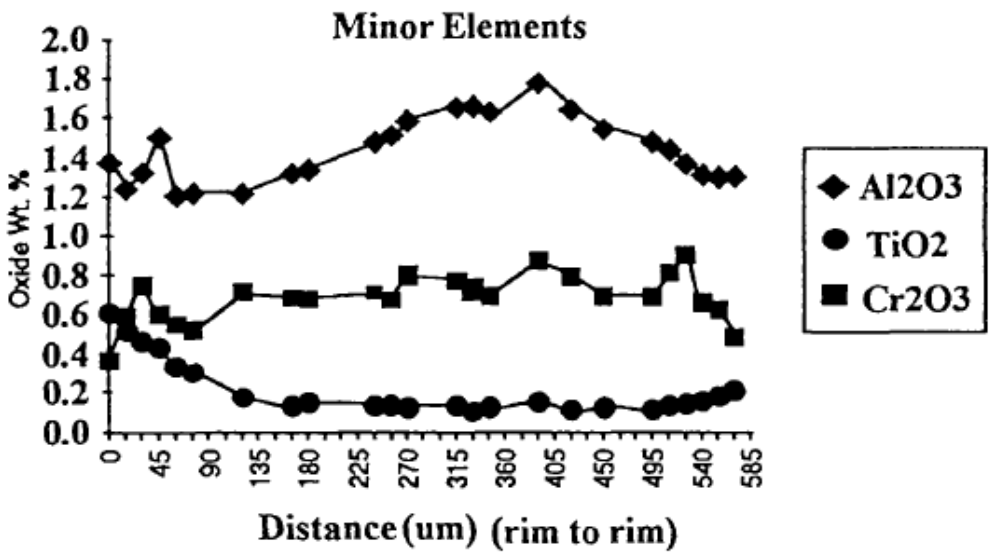


***Figure 16**: Minor element concentrations along a rim-to-rim transect in a Pasamonte pyroxene grain. Al and Cr decrease from core to rim, while Ti increases along the same path, especially at the rims. From Pun and Papike (1994).*

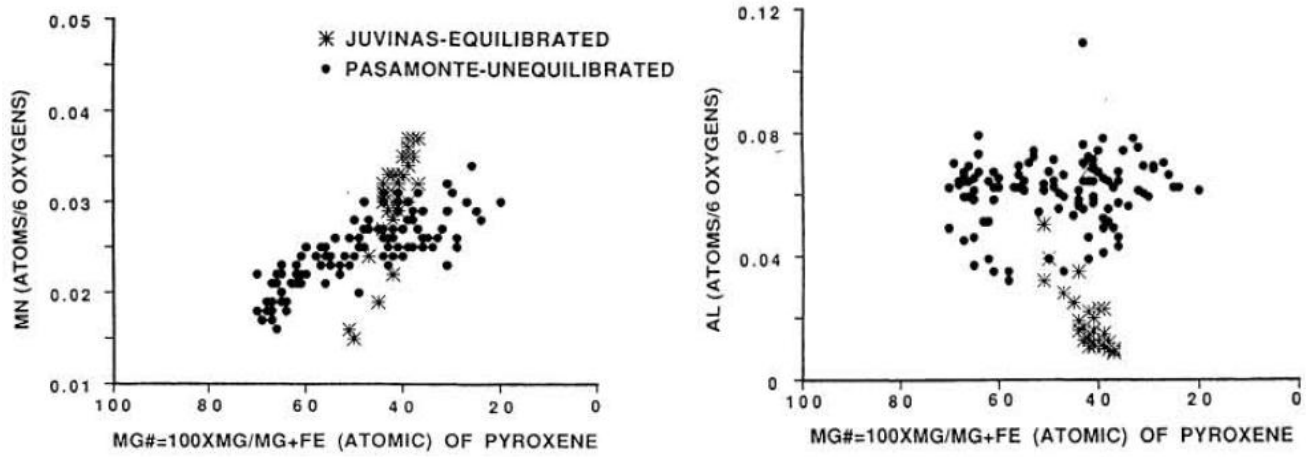


***Figure 17**: (a-left) Mn plotted against Mg# in Pasamonte pyroxenes, with Mn increasing as a function of decreasing Mg content. (b-right) Al plotted against Mg# in Pasamonte pyroxenes, showing higher Al content than most equilibrated eucrites (in this case Juvinas). Both figures from Buchanan and Reid (1992).*

In all of the above cases, $TiO_2$ (**Figure 16**), MnO (**Figure 17a**), and light lithophile elements like Li and B increase with decreases in Mg# (Takeda et al, 1978a; Reid and Barnard, 1979; BVSP, 1981; Buchanan and Reid, 1992; Pun and Papike, 1994; Herd et al, 2004), while $Cr_2O_3$ (**Figure 16**), Sc, Co, and Sm decrease in the same trend (BVSP, 1981; Phinney et al, 1993; Pun and Papike, 1994). Most pyroxenes in Pasamonte have a higher Al content than those found in unequilibrated pyroxenes (Buchanan and Reid, 1992; **Figure 17b**); some authors report no evidence of Al zoning (e.g. Buchanan and Reid, 1992) but others show slight Al decreases from core to rim (Pun and Papike, 1994; **Figure 16**). Both Type 1 and Type 2 zoning have been observed in single crystals, especially in lithic clasts that preserve an ophitic texture (Miyamoto et al, 1985; **Figure 18**), and Type 3 and 4 zoning is present in fractures of grains with Type 1 and 2 zoning (Schwartz and McCallum, 2005). Trace element analyses of Pasamonte pyroxene reveal clear LREE-depletion, a large negative Eu anomaly, and HREE-enrichment, with cores showing significant depletion relative to rims (Pun et al, 1992b; Pun and Papike, 1994; **Figure 19**), though relative REE concentrations in different grains vary by up to two orders of magnitude (Hsu and Crozaz, 1996).

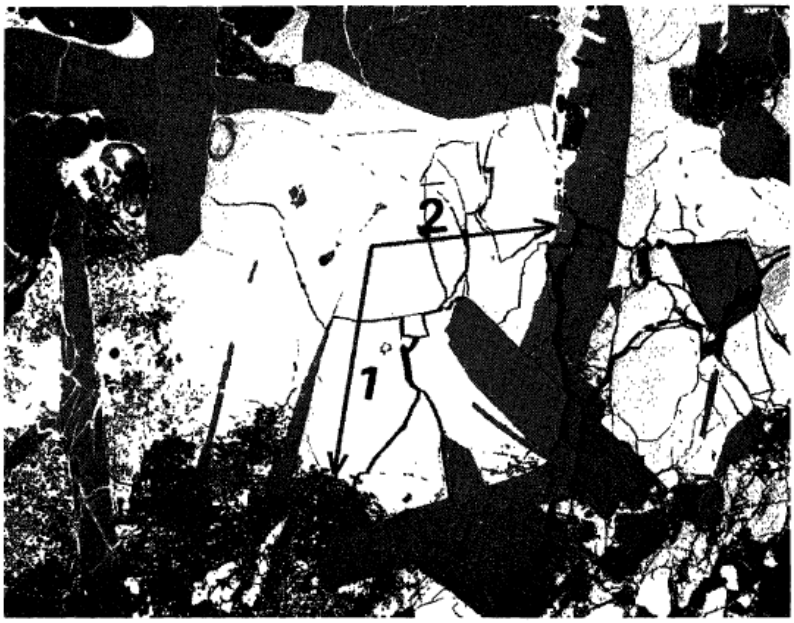


***Figure 18**: Type 1 and 2 zoning observed in the same pyroxene crystal, from Miyamoto et al (1985); transect 1 ends in a mesostasis and transect 2 terminates in a plagioclase lath.*

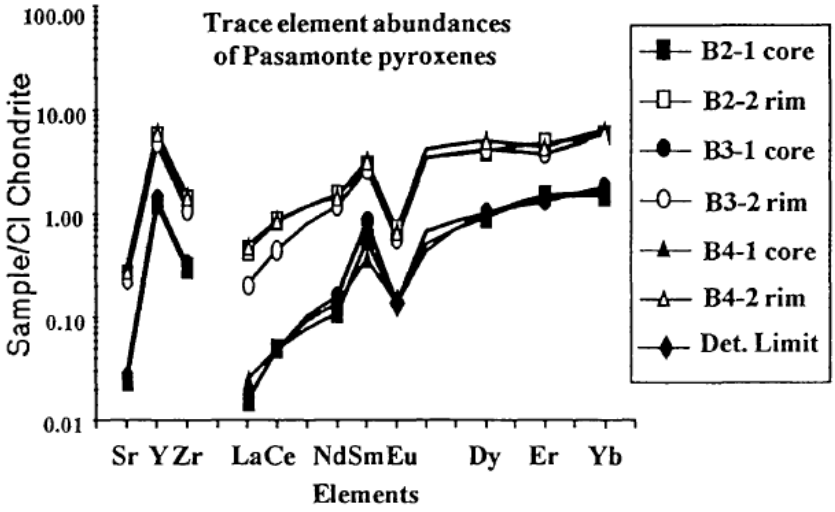


***Figure 19**: Trace element and REE abundances in Pasamonte pyroxene cores and rims, plotted relative to CI chondrites, from Pun and Papike (1994).*

Exsolution lamellae were not reported in Pasamonte pyroxenes by early authors (e.g. Foshag, 1938; Duke and Silver, 1967) as they are generally submicroscopic. However, they were later detected in the unequilibrated pigeonites using X-ray diffraction and TEM analysis, revealing (001) augite lamellae with a width of ≤0.2 µm (Takeda et al, 1976a, 1976b; Schwartz et al, 2002; **Figure 20**) as well as rare thin (100) augites (Brearley et al, 1993). Average widths and wavelengths vary from core to rim: Brearley et al (1993) reported 70 nm lamellae in pigeonite cores with a wavelength of 200 nm, whereas coarser 120 nm lamellae in the rims have a higher wavelength at 270 nm, reflecting either different cooling histories (Brearley et al, 1993) or preferential lamellae coarsening in Fe-rich pyroxenes associated with the late cryptic metasomatism (Schwartz and McCallum, 2005). (001) pigeonite lamellae have also been reported in late augites (Takeda et al, 1976b). Equilibrated pyroxenes, however, do show visible exsolution lamellae (up to 5 µm in size), and are usually coarser-grained (Metzler et al, 1994, 1995; Hsu and Crozaz, 1996).

***Figure 20**: TEM image of (001) augite lamellae (dark) in Pasamonte pigeonite (light); these lamellae have a wavelength of 225 nm. From Schwartz et al (2002).*

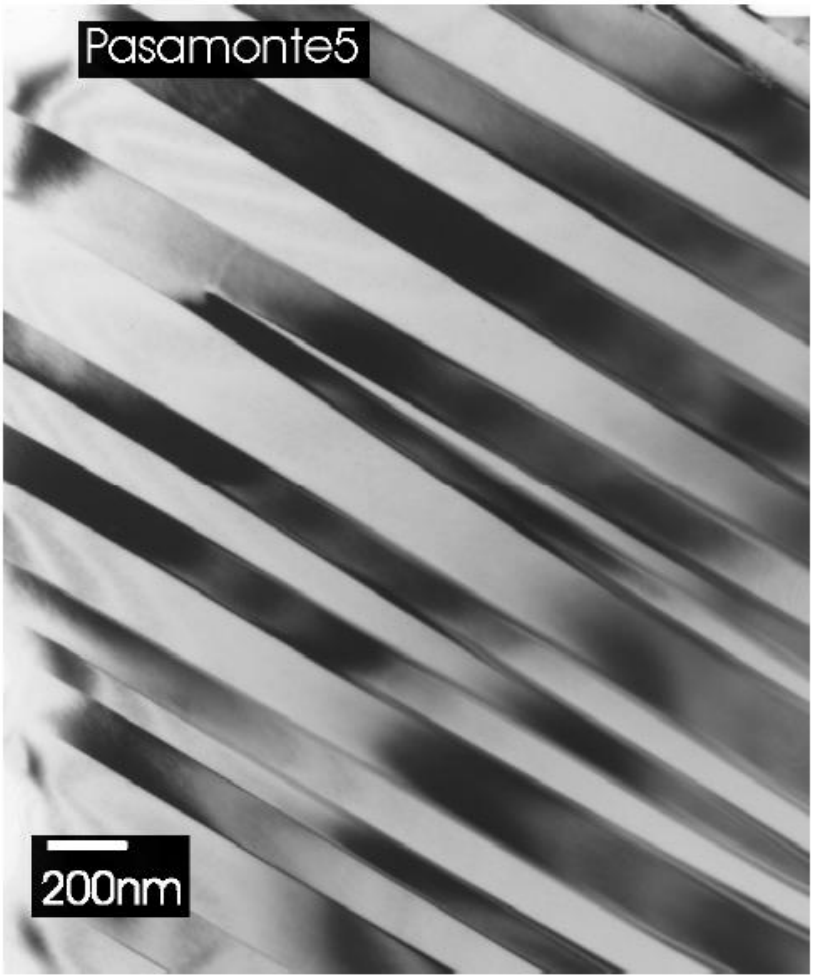


No clouding phases were observed in most Pasamonte pyroxenes, though some opaque phases have been reported in cracks in FeO-rich grains and rims (Harlow and Klimentidis, 1980); however, most fractures and cracks are free of late-deposited phases, leading Schwartz and McCallum (2005) to conclude that the late metasomatism experienced by Pasamonte was accompanied by a "dry" vapor rather than a fluid. The lack of pyroxene clouding may be related to low FeO concentrations in pigeonite cores relative to other eucrites, but also implies that Pasamonte experienced "a lesser degree of metamorphism or more rapid cooling" than the other eucrites (Harlow and Klimentidis, 1980).

(For a discussion of the thermal and metamorphic history that is responsible for the chemistry and textures of Pasamonte pyroxenes, refer to the "Metamorphism" section near the end of this paper.)

*Plagioclase.* Plagioclase feldspar in Pasamonte is found in both lithic clasts and the groundmass; it ranges from glassy to pure white, with irregular to conchoidal fracture and some Carlsbad twinning (Foshag, 1938). Many grains are clear but the majority (especially large grains) show minute, birefringent grains oriented in planes, chains, or rhombs (Foshag, 1938) which were later determined to be ilmenite, chromite, and Fe-metal, the latter of which is in greater abundances than plagioclase from most other eucrites (Harlow and Klimentidis, 1980). This limited plagioclase clouding, coupled with the absence of clouding in pyroxene, suggests lower-temperature metamorphism that occurred over a shorter period of time relative to other eucrites (Harlow and Klimentidis, 1980).

Compositionally, Pasamonte plagioclase is generally $An_{80-95}$, with a substantial amount of variability between clasts and some outliers (Foshag, 1938; Duke and Silver, 1967; Reid and Barnard, 1979; Harlow and Klimentidis, 1980; BVSP, 1981; Steele and Smith, 1982; **Figures 21 & 22**), low but detectable amounts of Ti, Fe, and Mg (BVSP, 1981), and apparent departures from stoichiometry (Reid and Barnard, 1979; BVSP, 1981). Like pyroxene, some Pasamonte plagioclase is zoned, with reverse zoning present as well (Duke and Silver, 1967; O'Neill and Delaney, 1982; Batchelor, 1991; Hsu and Crozaz, 1996; **Figure 23**); Steele and Smith (1982) reported an increase in Li, K, Sr, Ba, and Ti content in more evolved (i.e.,

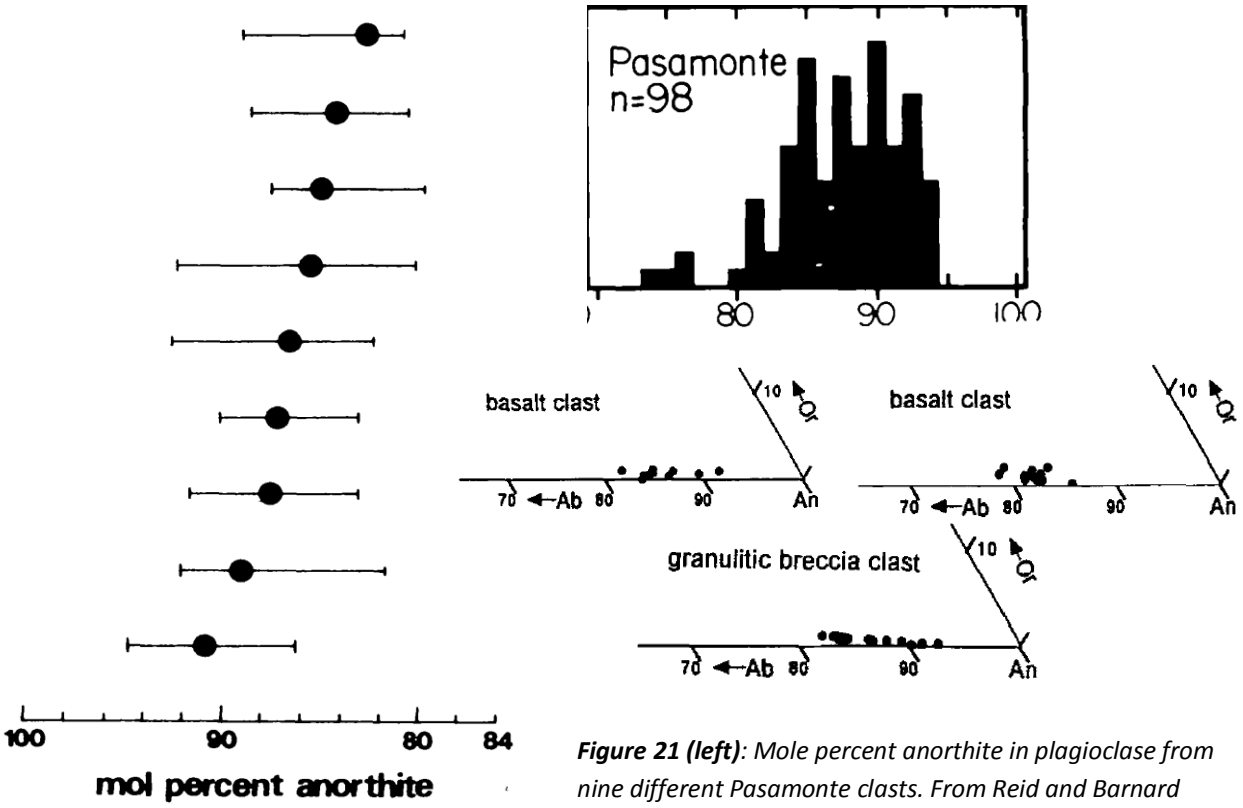


***Figure 21 (left)**: Mole percent anorthite in plagioclase from nine different Pasamonte clasts. From Reid and Barnard (1979), who interpreted these differences as a reflection of the unequilibrated nature of the eucrite; however, it also strongly supports the Metzler et al (1994, 1995) contention that Pasamonte is polymict. **Figure 22 (right)**: Histogram of mole percent anorthite for random plagioclase grains in Pasamonte, with significant variability, from Steele and Smith (1982). Also included are various plagioclase compositions from three different Pasamonte lithic clasts, from Metzler et al (1995).*

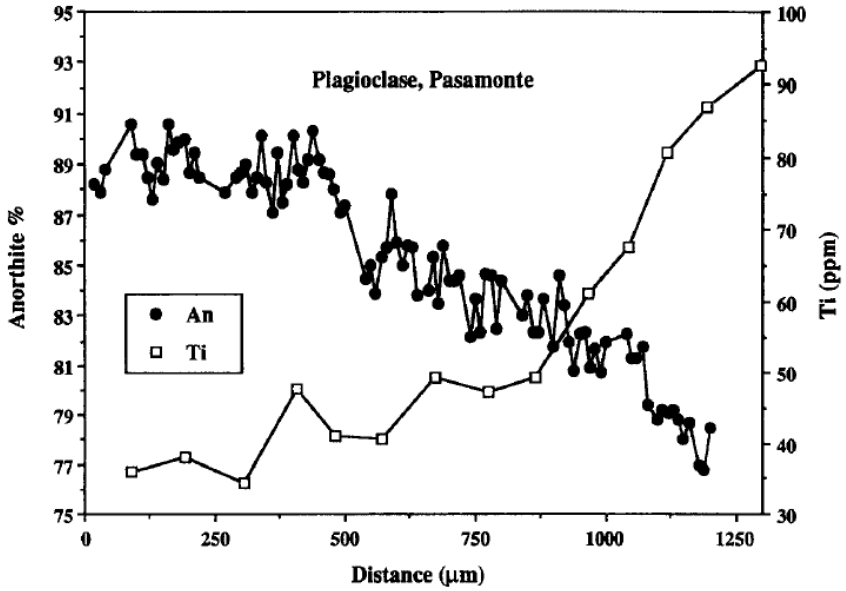


***Figure 23**: Major (An) and trace (Ti) element zoning in a single Pasamonte plagioclase grain, indicative of original igneous zoning. From Hsu and Crozaz (1996).*

Na-rich) compositions, and Hsu and Crozaz (1996) noted REE concentrations that increased 2-3x toward plagioclase rims. The relatively high Al contents of Pasamonte pyroxenes (see above) could imply that plagioclase nucleation was suppressed during early pyroxene nucleation and growth (Takeda et al, 1978a), though calculated melt compositions in equilibrium with both plagioclase and pyroxene cores indicate simultaneous crystallization (Hsu and Crozaz, 1996).

*Tridymite.* Tridymite was initially recognized in light mineral separates from Pasamonte as a glassy, colorless phase, some with an extremely high density of highly-birefringent inclusions that are as yet unidentified (Foshag, 1938). Pasamonte tridymite occurs as late-formed grains in both lithic and mineral clasts (Duke and Silver, 1967; Schwartz and McCallum, 2005); these crystals show patchy, streaky, and hackly extinctions with fine banding and conchoidal fracture (Foshag, 1938). A chemical analysis of Pasamonte tridymite showed 95.5% silica, though this determination was contaminated by pigeonite and the inclusions, so silica contents are likely higher (Foshag, 1938).

A cathodoluminescence study of Pasamonte showed two different silica populations, one associated with larger, euhedral, fractured laths that luminesced blue-green, versus a dull-red luminescing, anhedral population (Batchelor, 1991). Those that luminesced blue-green were interpreted as a high-grade, plutonic form, while the dull-red luminescing fraction was inferred to be a lower temperature variety, possibly a product of pyroxene reduction (Batchelor, 1991). The latter conclusion is supported by the observation of tridymite that formed from the decomposition of clinopyroxene at pigeonite rims to orthopyroxene, augite, and silica (Hsu and Crozaz, 1996).

*Mesostasis.* Mesostasis, or preserved fractions of the primary melt, is present in variable amounts in lithic clasts from the Pasamonte eucrite (BVSP, 1981). Pasamonte mesostasis shows high bulk $SiO_2$ and FeO content (Mg# = 22), and contains crystals of silica, ilmenite, Fe-Ni metal, FeS, and apatite, with small Ca-rich pyroxenes and plagioclase (Miyamoto et al, 1985). Small, 10-20 μm, fayalitic olivines, associated with high-Ca pyroxene and silica, were found in mesostasis from ophitic clasts; these were probably produced by the most fractionated stages of the liquid (Miyamoto et al, 1985). A chemical analysis of five Pasamonte mesostasis samples found flat REE patterns with 15-100x chondritic enrichment and a large negative Eu anomaly; two samples were very similar in bulk chemistry to the highly-fractionated eucrites Lakangaon and Nuevo Laredo, and thus may be representative of residual liquids (Phinney et al, 1993).

*Ilmenite.* Ilmenite is present in Pasamonte as *(1)* clouding inclusions in larger plagioclase grains (Harlow and Klimentidis, 1980), *(2)* free grains in the matrix (Harlow and Klimentidis, 1980), and *(3)* small crystals in mesostasis (Miyamoto et al, 1985). It is found in both mineral and lithic clasts (Schwartz and McCallum, 2005). Analyses of "free" ilmenite grains show 51-53% $TiO_2$ and an average Mg# of 2 (Bunch and Keil, 1971; Harlow and Klimentidis, 1980).

*Chromite.* Chromite occurs in Pasamonte as both "free" grains in the matrix and as inclusions in plagioclase (Harlow and Klimentidis, 1980); though the two types have similar Fe/Mg abundances (Mg# = 4-9), they have markedly different Cr/Cr+Al ratios (79 for inclusions and 66 for "free" grains) (Harlow and Klimentidis, 1980). As a whole, Pasamonte chromites are rather exceptional for eucrites, with a very high $Al_2O_3$ (9-18 wt. % vs 7-9% in other eucrites) and very low $TiO_2$ (1-3 wt. % vs. 3-6% in other eucrites) (Bunch and Keil, 1971; Harlow and Klimentidis, 1980; Scott et al, 2009).

*Troilite.* Troilite occurs in Pasamonte as *(1)* inclusions in Fe-rich pyroxene rims, *(2)* in mesostasis from lithic clasts, and *(3)* as an accessory mineral in mineral clasts (Duke and Silver, 1967; BVSP, 1981;

Miyamoto et al, 1985; Schwartz and McCallum, 2005). No detailed chemical analyses of Pasamonte troilite have been published in the literature.

*Phosphates.* At least three phosphate minerals have been identified in Pasamonte: *(1)* apatite that occurs in the mesostasis (Miyamoto et al, 1985), *(2)* fluorapatite (Hsu and Crozaz, 1996), and *(3)* whitlockite that occurs in lithic clasts (Schwartz and McCallum, 2005). REE analysis of the second occurrence, fluorapatite, shows the lowest REE abundances for any phosphate measured within the same study, as well as a relative LREE depletion (Hsu and Crozaz, 1996; **Figure 24**).

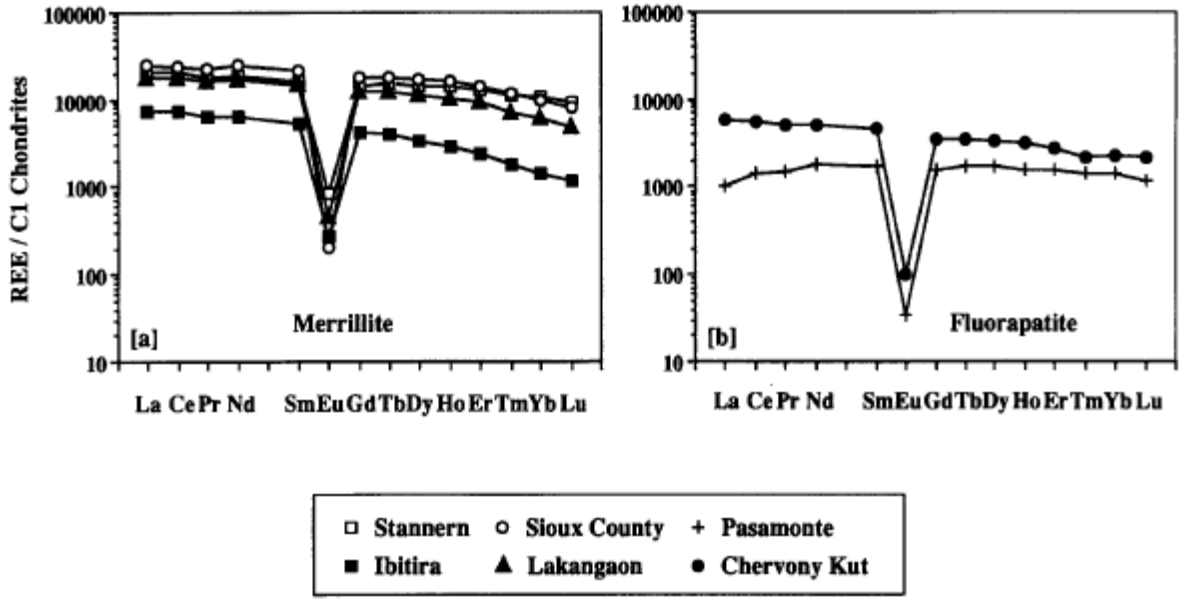


***Figure 24****: REE abundances in phosphates from six different eucrites; Pasamonte is represented by fluorapatite on the right diagram. Notice the relative LREE depletion in Pasamonte phosphates, which also have the lowest overall REE abundance. From Hsu and Crozaz (1996).*

*Olivine.* Fe-rich (Mg# ≈ 10), fayalitic olivines with minor CaO (0.30 wt%) and MnO (1.55 wt%) have been reported in Pasamonte mesostasis (Miyamoto et al, 1985); no other chemical analyses of Pasamonte olivines are available in the literature. A more recent study noted their varied occurrence in both mineral and lithic clasts, indicative of Fe-rich metasomatism and decomposition from metastable forbidden-zone pyroxene compositions (Schwartz et al, 2002; Schwartz and McCallum, 2005).

*Zircon.* Zircons occur in Pasamonte in association with ilmenite and chromite, and are usually less than 10 µm in diameter (Bukovanska and Ireland, 1993). U concentrations were found to be near 300 ppm, which was significantly higher than those measured in other eucrites (50-100 ppm), while REE were similar to meteoritic values, with an extreme HREE enrichment (Bukovanska and Ireland, 1993).

*Metal.* Foshag (1938) first noted the presence of metal in Pasamonte pigeonite grains; he found no obvious nickel-iron in lithic fragments or the groundmass, but noted that some pigeonites had dark included grains that were readily attracted to hand magnet. Other authors have noted the presence of Fe-Ni metal in Pasamonte mesostasis (Miyamoto et al, 1985), and most recently Ni-bearing metal particles were reported in a granulitic breccia clast (Metzler et al, 1995). This specific clast shows siderophile element enrichment indicative of chondritic contamination, with an especially high W

content, and thus these metal particles may originate from a metal-rich impact melt (Metzler et al, 1995; see **Figure 7**). No direct chemical analyses of Pasamonte Fe-Ni metal have been reported.

*Other.* Some Zr-rich minerals other than zircon have been identified in Pasamonte, most notably baddeleyite and zirconolite (Bukovanska and Ireland, 1993; Schwartz and McCallum, 2005). A chemical analysis of a 10-µm sized baddeleyite grain indicated similar uranium contents to meteoritic zircon (~60 ppm) and a slight LREE-enriched pattern (La = 1800xCI vs. Lu = 800xCI), with a large negative Eu anomaly (Bukovanska and Ireland, 1993).

**Whole Rock Composition**: Major and minor element analyses of bulk Pasamonte samples are shown in **Table 2**, while trace elements are shown in **Table 3**, with REE plotted relative to chondrites in **Figure 25**. In terms of whole-rock chemistry, future workers should be careful when determing "bulk" abundances for Pasamonte; many of the chemical investigations undertaken prior to 1994 were working on the assumption that Pasamonte was a monomict eucrite, and there are significant variations in many published values. This may reflect the selection of samples that are unrepresentative of the meteorite as a whole, though it may also be related to the unequilibrated, heterogenous nature of many of the clasts. An examination of the Metzler et al (1994, 1995) data (major, minor, and trace) reveals stark chemical differences between three separate clasts, two of which are unequilibrated (subophitic and variolitic basalt clasts); this is clear evidence that Pasamonte is polymict. REE data from these clasts is plotted separately in **Figure 26**; each clast is REE-enriched to a differing degree, with a negative Eu anomaly, but the unequilibrated clasts show relative LREE enrichment compared to HREE enrichment in the equilibrated granulitic breccia.

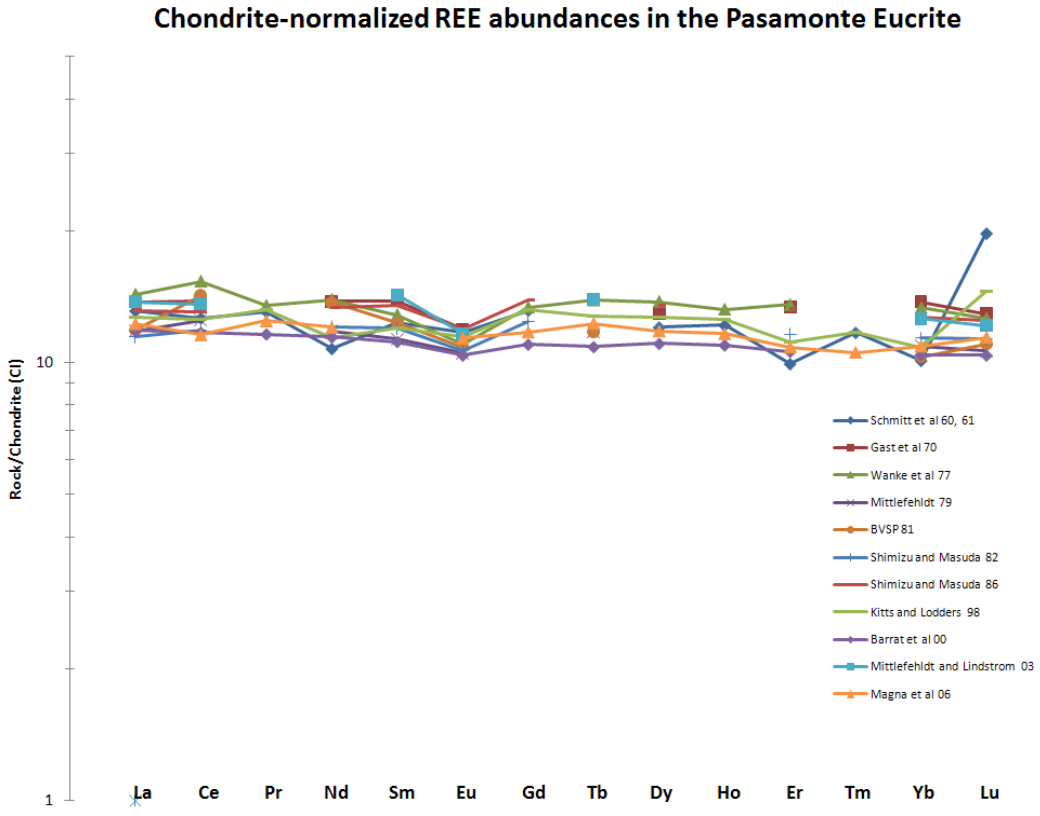


***Figure 25**: Chondrite-normalized whole-rock REE abundances in Pasamonte; the reference chondrite (CI) is from Evensen et al (1978).*

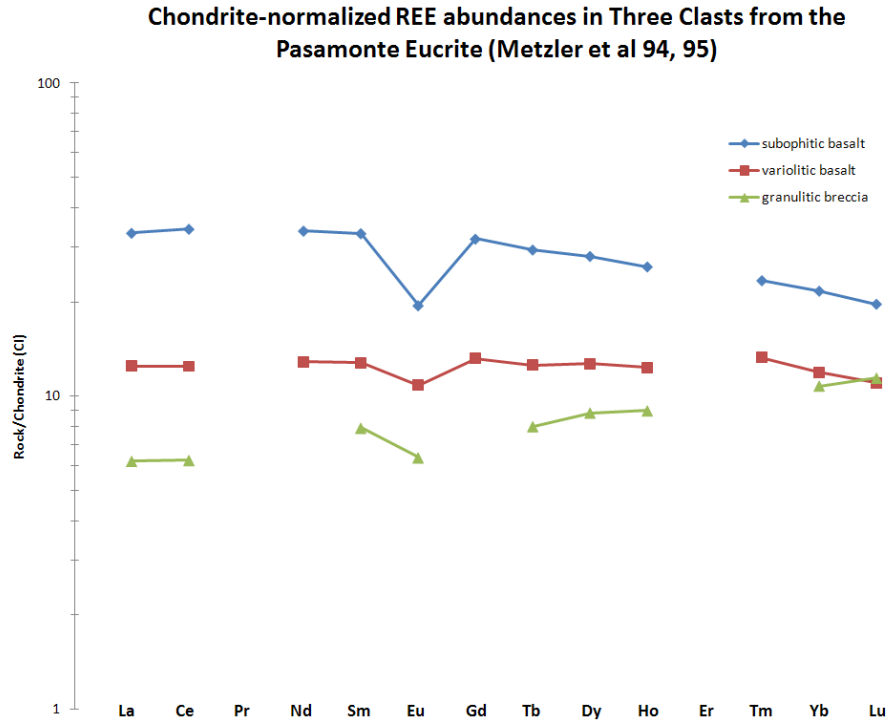


**Figure 26**: Chondrite-normalized REE abundances from three separated clasts, reported in Metzler et al (1994, 1995). The subophitic basalt (blue) and the variolitic basalt (red) are unequilibrated, while the granulitic breccia (green) is equilibrated; the basalt clasts shows relative LREE enrichment, while the granulitic breccia shows HREE enrichment. All clasts show a negative Eu anomaly. Siderophile element data indicates that the granulite breccia is contaminated with projectile material, most likely a chondrite (see **Figure 7**).

Volatile contents in Pasamonte were investigated by Gooding et al (1990); their analysis found no measurable water (contrary to Duke and Silver, 1967) but detected trace amounts of $CO_2$, CO, saturated and unsaturated hydrocarbons (indicative of terrestrial contamination), Cl, and HCl in both exterior and interior samples from the meteorite. However, $CO_2$ and CO release profiles (i.e., over increasing temperature) are associated with the release of hydrocarbons, indicating that the "apparent carbonate" in Pasamonte is likely related to terrestrial organic contamination (Gooding et al, 1990). Grady et al (1997) found similar results; while total C abundances in Pasamonte were determined to be near 500 ppm, most of this carbon was released during <600$^{o}$C oxidation of organic materials, and thus not representative of the actual meteorite. Carbon abundances measured at >600$^{o}$C, and thus assumed to be free of terrestrial contamination, were found to be significantly smaller (19 ppm) (Grady et al, 1997).

Chondritic contamination has been proposed in Pasamonte to explain enriched siderophile element abundances in a single granulite breccia clast (Metzler et al, 1995), Sm-Nd values that plot off the whole-eucrite isochron (Blichert-Toft et al, 2002) and anomalous whole-rock oxygen isotopic compositions that plot off the eucrite fractionation line (Wiechert et al, 2004; Greenwood et al, 2005; Scott et al, 2009; see section on oxygen isotopes, below). Both Wiechert et al (2004) and Greenwood et al (2005) posited that 1-3.5% chondritic material could explain oxygen isotopic compositions; however, though siderophile element abundances in Pasamonte are higher than most eucrites (Scott et al, 2009), simple admixing of 1% chondritic material would produce siderophile element concentrations that are ten times higher than those observed in Pasamonte (Wiechert et al, 2004). It is thus likely that while the single granulite breccia clast does indeed represent chondritic contamination (Metzler et al, 1995), the anomalous whole-rock oxygen isotopes are indicative of a Pasamonte parent body other than 4 Vesta (Scott et al, 2009).

**Table 2**: Major and minor element abundances (by weight) in the Pasamonte eucrite.

| reference | Foshag 38 | Duke and Silver 67 | von Michaelis et al 69b | McCarthy et al 73 | Bunch 75 | Fukuoka et al 77 |
|---|---|---|---|---|---|---|
| **comments** | | | | | single ophitic basalt clast | -- |
| **weight** | -- | -- | -- | -- | -- | -- |
| **$SiO_2$** | 48.20 | 48.59 | 47.88 | 48.07 | 52.0 | -- |
| **$TiO_2$** | 0.07 | 0.65 | 0.71 | 0.72 | 1.00 | 0.68 |
| **$Al_2O_3$** | 13.91 | 12.70 | 12.26 | 12.25 | 12.1 | 13.0 |
| **FeO** | 16.33 | 19.58 | 18.49 | 19.10 | 15.8 | 19.3 |
| **$Fe_2O_3$** | 0.79 | -- | -- | -- | -- | -- |
| **MnO** | 0.42 | 0.56 | 0.54 | 0.56 | 0.16 | 0.55 |
| **MgO** | 6.47 | 6.77 | 6.62 | 6.53 | 5.8 | 6.6 |
| **CaO** | 10.24 | 10.25 | 10.10 | 10.24 | 11.2 | 10.2 |
| **$Na_2O$** | 0.31 | 0.45 | -- | 0.51 | 0.70 | 0.45 |
| **$K_2O$** | 0.06 | 0.05 | 0.04 | 0.04 | 0.20 | 0.05 |
| **$Cr_2O_3$** | 0.30 | 0.33 | -- | 0.31 | -- | 0.3 |
| **$P_2O_5$** | -- | 0.10 | 0.11 | 0.11 | -- | -- |
| **S%** | 0.07 | -- | -- | -- | -- | -- |
| **FeS** | -- | 0.06 | -- | -- | -- | -- |
| **Fe (metal)** | 2.76 | -- | -- | -- | -- | -- |
| **$H_2O+$** | -- | 0.27 | -- | -- | -- | -- |
| **$H_2O-$** | -- | 0.01 | -- | -- | -- | -- |
| **sum (reported)** | **100.21** | **100.37** | **--** | **--** | **98.96** | **--** |
| **Mg#** | **41** | **38** | **39** | **38** | **40** | **38** |
| ***technique:*** | *wet chem.* | *wet chem.* | *wet chem.* | *wet chem.* | *EPMA* | *lit survey* |

| reference | Wanke et al 77 | Mittlefehldt 79 | Jochum et al 80 | BVSP 81 | Metzler et al 94, 95 | | | Kitts and Lodders 98 |
|---|---|---|---|---|---|---|---|---|
| | | | | | subophitic | variolitic | granulitic | |
| **comments** | -- | -- | -- | avg. of 4 clasts | basalt | basalt | breccia | -- |
| **weight** | -- | 83.0 mg | -- | -- | 10.2 mg | 28.2 mg | 14.8 mg | -- |
| **$SiO_2$** | 49.85 | -- | 50.70 | -- | -- | -- | -- | 49.10 |
| **$TiO_2$** | 0.75 | 0.78 | -- | 0.59 | 2.00 | 0.83 | 0.67 | 0.72 |
| **$Al_2O_3$** | 12.32 | 13.60 | 12.28 | 13.13 | 15.68 | 12.28 | 8.31 | 12.50 |
| **FeO** | 18.71 | 18.40 | 17.24 | 16.05 | 13.51 | 19.30 | 26.12 | 18.60 |
| **$Fe_2O_3$** | -- | -- | -- | -- | -- | -- | -- | -- |
| **MnO** | 0.55 | 0.52 | 0.48 | 0.48 | 0.33 | 0.54 | 0.63 | 0.53 |
| **MgO** | 6.00 | 3.98 | 6.47 | 7.10 | 3.65 | 6.63 | 9.45 | 6.50 |
| **CaO** | 10.32 | 10.08 | 10.36 | 11.13 | 10.36 | 9.94 | 7.70 | 10.30 |
| **$Na_2O$** | 0.51 | 0.64 | 0.43 | 0.52 | 0.56 | 0.72 | 0.34 | 0.49 |
| **$K_2O$** | 0.05 | 0.08 | 0.04 | -- | 0.05 | 0.08 | 0.02 | 0.04 |
| **$Cr_2O_3$** | 0.31 | 0.34 | 0.20 | 1.23 | 0.12 | 0.31 | 0.38 | 0.29 |
| **$P_2O_5$** | 0.08 | -- | -- | -- | -- | -- | -- | 0.10 |
| **S%** | 0.11 | -- | 0.04 | -- | -- | -- | -- | 0.08 |
| **FeS** | -- | -- | -- | -- | -- | -- | -- | -- |
| **Fe (metal)** | -- | -- | -- | -- | -- | -- | -- | -- |
| **$H_2O+$** | -- | -- | -- | -- | -- | -- | -- | -- |
| **$H_2O-$** | -- | -- | -- | -- | -- | -- | -- | -- |
| **sum (reported)** | **--** | **--** | **--** | **--** | **--** | -- | -- | **99.10** |
| **Mg#** | **36** | **28** | **40** | **44** | **33** | **38** | **39** | **38** |
| ***technique:*** | *XRF/INAA/RNAA* | *INAA* | *spark source MS* | *INAA* | *INAA* | *INAA* | *INAA* | *lit survey* |

**Table 3**: Trace element abundances in the Pasamonte eucrite.

| reference | Schmitt et al 63 | Ahrens 70 | Gast et al 70 | Ahrens and Danchin 71 | Chou et al 76 | Fukuoka et al 77 |
|---|---|---|---|---|---|---|
| weight | -- | -- | -- | -- | -- | -- |
| comments | *in* Mason 62 | -- | -- | -- | -- | -- |
| Sc ppm | -- | 26 (c) | -- | 26 (c) | -- | 33 (c) |
| V ppm | -- | -- | -- | -- | -- | -- |
| Co ppm | -- | -- | -- | 6 (c) | -- | 6 (c) |
| Ni ppm | -- | -- | -- | 9 (c) | 28 (d) | 5 (c) |
| Cu ppm | -- | -- | -- | 4 (c) | -- | -- |
| Zn ppm | -- | -- | -- | 2 (c) | 2.4 (d) | -- |
| Ga ppm | -- | -- | -- | 1 (c) | 2.0 (d) | -- |
| Ge ppm | -- | -- | -- | -- | 0.040 (d) | -- |
| As ppb | -- | -- | -- | -- | -- | -- |
| Se ppm | -- | -- | -- | -- | -- | -- |
| Rb ppm | -- | -- | 0.19 (b) | 0.25 (c) | -- | -- |
| Sr ppm | -- | 81 (c) | 56.6 (b) | 8.06 (c) | -- | 80 (c) |
| Y ppm | -- | -- | -- | -- | -- | -- |
| Zr ppm | -- | 58 (c) | -- | 58 (c) | -- | -- |
| Nb ppm | -- | -- | -- | -- | -- | -- |
| Mo ppb | -- | -- | -- | -- | -- | -- |
| Ru ppm | -- | -- | -- | -- | -- | -- |
| Rh ppm | -- | -- | -- | -- | -- | -- |
| Pd ppb | -- | -- | -- | -- | -- | -- |
| Ag ppb | -- | -- | -- | -- | -- | -- |
| Cd ppb | -- | -- | -- | -- | 47 (d) | -- |
| In ppb | -- | -- | -- | -- | 3.2 (d) | -- |
| Sn ppb | -- | -- | -- | -- | -- | -- |
| Sb ppb | -- | -- | -- | 24 (c) | -- | -- |
| Te ppb | -- | -- | -- | 0.3 (c) | -- | -- |
| Cs ppb | -- | -- | -- | 11 (c) | -- | -- |
| Ba ppm | -- | 29 (c) | 38.4 (b) | 32 (c) | -- | 30 (c) |
| La ppm | 3.21 (a) | -- | 3.36 (b) | 3.21 (c) | -- | 3.21 (c) |
| Ce ppm | 8.08 (a) | -- | 8.84 (b) | 8.08 (c) | -- | -- |
| Pr ppm | 1.26 (a) | -- | -- | 1.26 (c) | -- | -- |
| Nd ppm | 5.18 (a) | 5.18 (c) | 6.54 (b) | 5.18 (c) | -- | -- |
| Sm ppm | 1.9 (a) | -- | 2.13 (b) | 1.90 (c) | -- | 1.90 (c) |
| Eu ppm | 0.68 (a) | -- | 0.691 (b) | 0.68 (c) | -- | 0.68 (c) |
| Gd ppm | 2.69 (a) | -- | -- | 2.69 (c) | -- | -- |
| Tb ppm | -- | -- | -- | -- | -- | -- |
| Dy ppm | 3.06 (a) | -- | 3.29 (b) | 3.06 (c) | -- | -- |
| Ho ppm | 0.69 (a) | -- | -- | 0.69 (c) | -- | -- |
| Er ppm | 1.65 (a) | -- | 2.22 (b) | 1.64 (c) | -- | -- |
| Tm ppm | 0.3 (a) | -- | -- | 0.30 (c) | -- | -- |
| Yb ppm | 1.67 (a) | 1.67 (c) | 2.27 (b) | 1.67 (c) | -- | 1.67 (c) |
| Lu ppm | 0.5 (a) | -- | 0.328 (b) | 0.50 (c) | -- | 0.50 (c) |
| Hf ppb | -- | -- | -- | -- | -- | -- |
| Ta ppb | -- | -- | -- | 120 (c) | -- | -- |
| W ppb | -- | -- | -- | -- | -- | -- |
| Re ppb | -- | -- | -- | -- | -- | -- |
| Os ppb | -- | -- | -- | -- | -- | -- |
| Ir ppb | -- | -- | -- | 22 (c) | 0.65 (d) | -- |
| Pt ppb | -- | -- | -- | -- | -- | -- |
| Au ppb | -- | -- | -- | 2.5 (c) | 0.52 (d) | 0.5 (c) |
| Th ppb | ***Kuroda et al 66*** | 520 (c) | -- | 520 (c) | ***Fisher 73*** | -- |
| U ppb | *78.0 (a)* | 107 (c) | ***Quijano-Rico and Wanke 69*** | 107 (c) | *122 (c)* | -- |
| Li ppm | -- | -- | *6* | 6.0 (c) | -- | -- |
| Be ppm | -- | -- | -- | 0.039 (c) | -- | ***Curtis et al 80*** |
| B ppm | -- | -- | *1.08* | 1.2, 1.08 (c) | -- | *5.6 (a)* |
| S ppm | -- | -- | -- | -- | ***Dreibus et al 79*** | -- |
| F ppm | -- | -- | -- | -- | *52 (d)* | -- |
| Cl ppm | -- | -- | *8* | 13 (c) | *26 (d)* | -- |
| Br ppm | ***Kuroda et al 66*** | -- | -- | -- | *0.149 (d)* | -- |
| I ppb | *113.0 (a)* | -- | -- | 110 (c) | *60 (d)* | -- |
| Pb ppm | -- | -- | -- | -- | -- | -- |
| Hg ppb | -- | -- | -- | -- | -- | -- |
| Tl (ppb) | -- | -- | -- | -- | -- | -- |
| Bi (ppb) | -- | -- | -- | -- | -- | -- |

*technique: (a) INAA, (b) mass spectrometry, (c) lit survey, (d) RNAA*

**Table 3, cont.**: Trace element abundances in the Pasamonte eucrite.

| reference | Wanke et al 77 | Mittlefehldt 79 | Palme and Rammensee 81 | BVSP 81 | Shimizu and Masuda 82 |
|---|---|---|---|---|---|
| weight | -- | 83.0 mg | 234 mg | -- | -- |
| comments | -- | -- | -- | average of four clasts | -- |
| Sc ppm | 33.9 (a, d) | 31 (a) | 27.7 (a) | 22.5 (a) | -- |
| V ppm | 60.0 (a, d) | 59 (a) | -- | 69 (a) | -- |
| Co ppm | 6.92 (a, d) | 9.5 (a) | 4.4 (a) | 6 (a) | -- |
| Ni ppm | -- | -- | -- | -- | -- |
| Cu ppm | 17.5 (a, d) | -- | 0.9 (a) | -- | -- |
| Zn ppm | 12.8 (a, d) | -- | -- | -- | -- |
| Ga ppm | 1.73 (a, d) | -- | -- | -- | -- |
| Ge ppm | 0.06 (a, d) | -- | -- | -- | -- |
| As ppb | 120 (a, d) | -- | 13 (a) | -- | -- |
| Se ppm | 0.091 (a, d) | -- | -- | -- | -- |
| Rb ppm | 0.60 (a, d) | -- | -- | -- | -- |
| Sr ppm | 76 (a, d) | -- | -- | 75 (a) | -- |
| Y ppm | -- | -- | -- | -- | -- |
| Zr ppm | 54 (a, d) | -- | -- | -- | -- |
| Nb ppm | 10 (a, d) | -- | -- | -- | ***Newsom 84*** |
| Mo ppb | -- | -- | -- | -- | *27.1* |
| Ru ppm | -- | -- | -- | -- | -- |
| Rh ppm | -- | -- | -- | -- | -- |
| Pd ppb | -- | -- | -- | -- | -- |
| Ag ppb | -- | -- | -- | -- | -- |
| Cd ppb | -- | -- | -- | -- | -- |
| In ppb | -- | -- | -- | -- | -- |
| Sn ppb | -- | -- | -- | -- | -- |
| Sb ppb | -- | -- | 5 (a) | -- | -- |
| Te ppb | -- | -- | -- | -- | -- |
| Cs ppb | 50 (a, d) | -- | -- | -- | -- |
| Ba ppm | 37.2 (a, d) | -- | -- | 33 (a) | -- |
| La ppm | 3.50 (a, d) | 2.89 (a) | 3.01 (a) | 2.9 (a) | 2.80 (b) |
| Ce ppm | 9.8 (a, d) | 8.0 (a) | -- | 9.1 (a) | 7.57 (b) |
| Pr ppm | 1.3 (a, d) | -- | -- | -- | -- |
| Nd ppm | 6.6 (a, d) | 5.6 (a) | -- | 6.5 (a) | 5.72 (b) |
| Sm ppm | 1.98 (a, d) | 1.74 (a) | 1.74 (a) | 1.9 (a) | 1.844 (b) |
| Eu ppm | 0.64 (a, d) | 0.61 (a) | 0.63 (a) | 0.63 (a) | 0.617 (b) |
| Gd ppm | 2.73 (a, d) | -- | -- | -- | 2.54 (b) |
| Tb ppm | 0.52 (a, d) | 0.44 (a) | 1.87 (a) | 0.44 (a) | -- |
| Dy ppm | 3.50 (a, d) | -- | -- | -- | 3.06 (b) |
| Ho ppm | 0.75 (a, d) | -- | -- | -- | -- |
| Er ppm | 2.25 (a, d) | -- | -- | -- | 1.929 (b) |
| Tm ppm | -- | -- | -- | -- | -- |
| Yb ppm | 2.20 (a, d) | 1.80 (a) | -- | 1.7 (a) | 1.877 (b) |
| Lu ppm | 0.32 (a, d) | 0.27 (a) | 0.27 (a) | 0.28 (a) | 0.287 (b) |
| Hf ppb | 1590 (a, d) | 1300 (a) | 1350 (a) | 1400 (a) | -- |
| Ta ppb | 200 (a, d) | 170(a) | 216 (a) | 200 (a) | -- |
| W ppb | 93 (a, d) | -- | 38 (a) | -- | -- |
| Re ppb | 1.3 (a, d) | -- | -- | -- | -- |
| Os ppb | -- | -- | -- | -- | -- |
| Ir ppb | -- | -- | -- | -- | -- |
| Pt ppb | -- | -- | -- | -- | -- |
| Au ppb | 3.7 (a, d) | 5.1 (a) | 0.3 (a) | -- | -- |
| Th ppb | -- | 380 (a) | 295 (a) | 0.3 (a) | -- |
| U ppb | -- | -- | -- | -- | -- |
| Li ppm | 10 (a, d) | -- | -- | -- | -- |
| Be ppm | -- | -- | -- | -- | -- |
| B ppm | -- | ***Moore et al 80*** | ***Gibson et al 85*** | -- | -- |
| S ppm | -- | *480-1300* | *810* | -- | -- |
| F ppm | 52 (a, d) | -- | -- | -- | -- |
| Cl ppm | 26 (a, d) | *15* | -- | -- | -- |
| Br ppm | 0.149 (a, d) | -- | -- | -- | -- |
| I ppb | 56 (a, d) | -- | -- | -- | -- |
| Pb ppm | -- | -- | -- | -- | -- |
| Hg ppb | -- | -- | -- | -- | -- |
| Tl (ppb) | -- | -- | -- | -- | -- |
| Bi (ppb) | -- | -- | -- | -- | -- |

*technique: (a) INAA, (b) mass spectrometry, (c) lit survey, (d) RNAA*

**Table 3, cont.**: Trace element abundances in the Pasamonte eucrite.

| reference | Shimizu and Masuda 86 | Paul and Lipschutz 90 | | Metzler et al 94, 95 | |
|---|---|---|---|---|---|
| weight | -- | -- | 10.1 mg | 28.2 mg | 14.8 mg |
| comments | -- | average of 2 samples | subophitic basalt | variolitic basalt | granulitic basalt |
| Sc ppm | -- | -- | 24.2 (a) | 31.4 (a) | 36.2 (a) |
| V ppm | -- | -- | 29.0 (a) | 73.1 (a) | 82.8 (a) |
| Co ppm | -- | 3.94 (a) | 28.7 (a) | 6.20 (a) | 140 (a) |
| Ni ppm | -- | -- | <150 (a) | <10.0 (a) | 1480 (a) |
| Cu ppm | -- | -- | -- | -- | -- |
| Zn ppm | -- | 1.79 (a) | 33.0 (a) | 30.0 (a) | 30.0 (a) |
| Ga ppm | -- | 1.46 (a) | 2.40 (a) | 2.70 (a) | 2.20 (a) |
| Ge ppm | -- | -- | -- | -- | -- |
| As ppb | -- | -- | -- | -- | -- |
| Se ppm | -- | 30 (a) | <1.00 (a) | 0.60 (a) | <0.50 (a) |
| Rb ppm | -- | 0.210 (a) | -- | -- | -- |
| Sr ppm | 78.5 (b) | -- | 140 (a) | <110 (a) | 130 (a) |
| Y ppm | -- | -- | -- | -- | -- |
| Zr ppm | -- | -- | <150 (a) | 70.0 (a) | <50.0 (a) |
| Nb ppm | -- | -- | -- | -- | -- |
| Mo ppb | -- | -- | -- | -- | -- |
| Ru ppm | -- | -- | -- | -- | -- |
| Rh ppm | -- | -- | -- | -- | -- |
| Pd ppb | -- | -- | -- | -- | -- |
| Ag ppb | -- | 0.49 (a) | -- | -- | -- |
| Cd ppb | -- | 9.3 (a) | -- | -- | -- |
| In ppb | -- | 3.25 (a) | -- | -- | -- |
| Sn ppb | -- | -- | -- | -- | -- |
| Sb ppb | -- | 1.4 (a) | -- | -- | -- |
| Te ppb | -- | 5.2 (a) | -- | -- | -- |
| Cs ppb | -- | 12 (a) | -- | -- | -- |
| Ba ppm | 34.6 (b) | -- | <50.0 (a) | 21.0 (a) | <50.0 (a) |
| La ppm | 3.22 (b) | -- | 8.13 (a) | 3.05 (a) | 1.52 (a) |
| Ce ppm | 8.36 (b) | -- | 21.9 (a) | 7.97 (a) | 4.00 (a) |
| Pr ppm | -- | -- | -- | -- | -- |
| Nd ppm | 6.32 (b) | -- | 16.0 (a) | 6.10 (a) | -- |
| Sm ppm | 2.08 (b) | -- | 5.10 (a) | 1.97 (a) | 1.22 (a) |
| Eu ppm | 0.691 (b) | -- | 1.13 (a) | 0.63 (a) | 0.37 (a) |
| Gd ppm | 2.84 (b) | -- | 6.50 (a) | 2.70 (a) | -- |
| Tb ppm | -- | -- | 1.10 (a) | 0.47 (a) | 0.30 (a) |
| Dy ppm | 3.44 (b) | -- | 7.12 (a) | 3.23 (a) | 2.25 (a) |
| Ho ppm | -- | -- | 1.47 (a) | 0.70 (a) | 0.51 (a) |
| Er ppm | 2.20 (b) | -- | -- | -- | -- |
| Tm ppm | -- | -- | 0.60 (a) | 0.34 (a) | -- |
| Yb ppm | 2.09 (b) | -- | 3.58 (a) | 1.97 (a) | 1.78 (a) |
| Lu ppm | 0.316 (b) | ***Quitte et al 00*** | 0.50 (a) | 0.28 (a) | 0.29 (a) |
| Hf ppb | -- | *1652 (b)* | 4010 (a) | 1410 (a) | 1080 (a) |
| Ta ppb | -- | -- | 710 (a) | 200 (a) | 140 (a) |
| W ppb | -- | *82.3 (b)* | <350 (a) | <150 (a) | 900 (a) |
| Re ppb | -- | -- | -- | -- | -- |
| Os ppb | -- | -- | -- | -- | -- |
| Ir ppb | -- | -- | <2 (a) | <2 (a) | 68 (a) |
| Pt ppb | -- | **Paul and Lipschutz 90** | -- | -- | -- |
| Au ppb | -- | 0.07 (a) | <5 (a) | <1 (a) | 21 (a) |
| Th ppb | -- | -- | 1000 (a) | 400 (a) | <250 (a) |
| U ppb | -- | 94 (a) | 250 (a) | 120 (a) | <35 (a) |
| Li ppm | -- | -- | -- | -- | -- |
| Be ppm | -- | -- | -- | -- | -- |
| B ppm | -- | -- | -- | -- | -- |
| S ppm | -- | -- | -- | -- | -- |
| F ppm | -- | -- | -- | -- | -- |
| Cl ppm | -- | -- | -- | -- | -- |
| Br ppm | -- | -- | -- | -- | -- |
| I ppb | -- | -- | -- | -- | -- |
| Pb ppm | -- | -- | -- | -- | -- |
| Hg ppb | -- | -- | -- | -- | -- |
| Tl (ppb) | -- | 0.29 (a) | -- | -- | -- |
| Bi (ppb) | -- | 1.1 (a) | -- | -- | -- |

*technique: (a) INAA, (b) mass spectrometry, (c) lit survey, (d) RNAA*

**Table 3, cont.**: Trace element abundances in the Pasamonte eucrite.

| reference | Kitts and Lodders 98 | Barrat et al 00 | Mittlefehldt and Lindstrom 03 | Magna et al 06 |
|---|---|---|---|---|
| weight | -- | 108.92 mg | 47.36 mg | -- |
| comments | -- | -- | -- | -- |
| Sc ppm | 31.5 (c) | 28.6 (b) | 32.4 (a) | 29.3 (b) |
| V ppm | 70 (c) | -- | -- | -- |
| Co ppm | 5.0 (c) | 8.9 (b) | 5.81 (a) | 7.5 (b) |
| Ni ppm | 12 (c) | 1.9 (b) | -- | 22 (b) |
| Cu ppm | 2.45 (c) | 5.1 (b) | -- | 2.3 (b) |
| Zn ppm | 2.0 (c) | 6.1 (b) | -- | -- |
| Ga ppm | 1.65 (c) | 1.96 (b) | -- | 2.9 (b) |
| Ge ppm | 0.035 (c) | -- | -- | -- |
| As ppb | 0.067 (c) | -- | -- | -- |
| Se ppm | 0.05 (c) | -- | -- | -- |
| Rb ppm | 0.24 (c) | 1.04 (b) | -- | 0.40 (b) |
| Sr ppm | 76.7 (c) | 78 (b) | 98 (a) | 79 (b) |
| Y ppm | 17 (c) | 17.54 (b) | -- | 17 (b) |
| Zr ppm | 57 (c) | 48.49 (b) | -- | 48 (b) |
| Nb ppm | 3.6 (c) | 3.25 (b) | -- | 3.9 (b) |
| Mo ppb | 27 (c) | -- | -- | -- |
| Ru ppm | -- | -- | -- | -- |
| Rh ppm | -- | -- | -- | -- |
| Pd ppb | -- | -- | -- | -- |
| Ag ppb | 0.49 (c) | -- | -- | -- |
| Cd ppb | 28.2 (c) | -- | -- | -- |
| In ppb | 3.23 (c) | -- | -- | -- |
| Sn ppb | -- | -- | -- | -- |
| Sb ppb | 3.2 (c) | -- | -- | -- |
| Te ppb | 5.1 (c) | -- | -- | -- |
| Cs ppb | 109 (c) | 58 (b) | -- | 10 (b) |
| Ba ppm | 32.5 (c) | 36.3 (b) | 36 (a) | 32 (b) |
| La ppm | 3.106 (c) | 2.90 (b) | 3.37 (a) | 3.0 (b) |
| Ce ppm | 8.043 (c) | 7.50 (b) | 8.7 (a) | 7.4 (b) |
| Pr ppm | 1.273 (c) | 1.12 (b) | -- | 1.2 (b) |
| Nd ppm | 5.413 (c) | 5.42 (b) | -- | 5.7 (b) |
| Sm ppm | 1.844 (c) | 1.72 (b) | 2.20 (a) | 0.86 (b) |
| Eu ppm | 0.663 (c) | 0.603 (b) | 0.675 (a) | 0.66 (b) |
| Gd ppm | 2.700 (c) | 2.25 (b) | -- | 2.4 (b) |
| Tb ppm | 0.477 (c) | 0.407 (b) | 0.523 (a) | 0.46 (b) |
| Dy ppm | 3.232 (c) | 2.81 (b) | -- | 3.0 (b) |
| Ho ppm | 0.71 (c) | 0.622 (b) | -- | 0.66 (b) |
| Er ppm | 1.853 (c) | 1.76 (b) | -- | 1.8 (b) |
| Tm ppm | 0.3 (c) | -- | -- | 0.27 (b) |
| Yb ppm | 1.785 (c) | 1.72 (b) | 2.08 (a) | 1.8 (b) |
| Lu ppm | 0.37 (c) | 0.264 (b) | 0.308 (a) | 0.29 (b) |
| Hf ppb | 1240 (c) | 1250 (b) | 1600 (a) | 1100 (b) |
| Ta ppb | 169 (c) | 184 (b) | 168 (a) | -- |
| W ppb | 38 (c) | 71 (b) | -- | -- |
| Re ppb | -- | -- | -- | -- |
| Os ppb | -- | -- | -- | -- |
| Ir ppb | 0.62 (c) | -- | -- | -- |
| Pt ppb | -- | -- | -- | -- |
| Au ppb | 0.30 (c) | -- | -- | -- |
| Th ppb | 355 (c) | 408 (b) | 370 (a) | -- |
| U ppb | 92 (c) | 127 (b) | -- | 90 (b) |
| Li ppm | 9 (c) | -- | -- | 10.1 (b) |
| Be ppm | 0.039 (c) | -- | -- | -- |
| B ppm | 3.34 (c) | -- | -- | -- |
| S ppm | -- | -- | -- | -- |
| F ppm | 42 (c) | -- | -- | -- |
| Cl ppm | 16 (c) | -- | -- | -- |
| Br ppm | 0.149 (c) | -- | -- | -- |
| I ppb | 108 (c) | -- | -- | -- |
| Pb ppm | 0.289 (c) | -- | -- | 0.31 (b) |
| Hg ppb | -- | -- | -- | -- |
| Tl (ppb) | 0.29 (c) | -- | -- | -- |
| Bi (ppb) | 1.1 (c) | -- | -- | -- |

*technique: (a) INAA, (b) mass spectrometry, (c) lit survey, (d) RNAA*

**Radiogenic Isotopes**: Radiogenic isotope work on Pasamonte is rather extensive, and covers a number of isotopic systems; as such, each age-dating system is treated separately, with a short summary at the end. It is important to consider that many of these researchers, especially those prior to the revisions of Metzler et al (1994, 1995), assumed that Pasamonte was a monomict eucrite.

*Rb-Sr/Sr-Sr*. Early literature Rb-Sr ages from mineral separates in Pasamonte were reported by Goles et al (1960), with values ranging from 4.4-4.6 Ga. Anders (1963) replotted Rb-Sr data from Goles et al (1960) to determine a slightly younger Pasamonte age of 4.37 Ga (also referenced in Rowe and Kuroda, 1965). This age is strikingly similar to the 4.39 ± 0.26 Ga whole-eucrite isochron published in the classic Sr isotopic study of Papanastassiou and Wasserburg (1969).

More recent analyses have suggested that the Rb-Sr system was disturbed between 2.5-2.9 Ga (Birck and Allegre, 1978), and probably very recently as well (Unruh et al, 1977), as Pasamonte data do not define a statistically significant isochron (Nakamura et al, 1976; Unruh et al, 1977; Birck and Allegre, 1978; **Figure 27**). However, tie lines connecting plagioclase and whole rock data from Pasamonte give an age of 4.55-4.59 Ga, suggesting that the meteorite crystallized near this age (Unruh et al, 1977; Birck and Allegre, 1978).

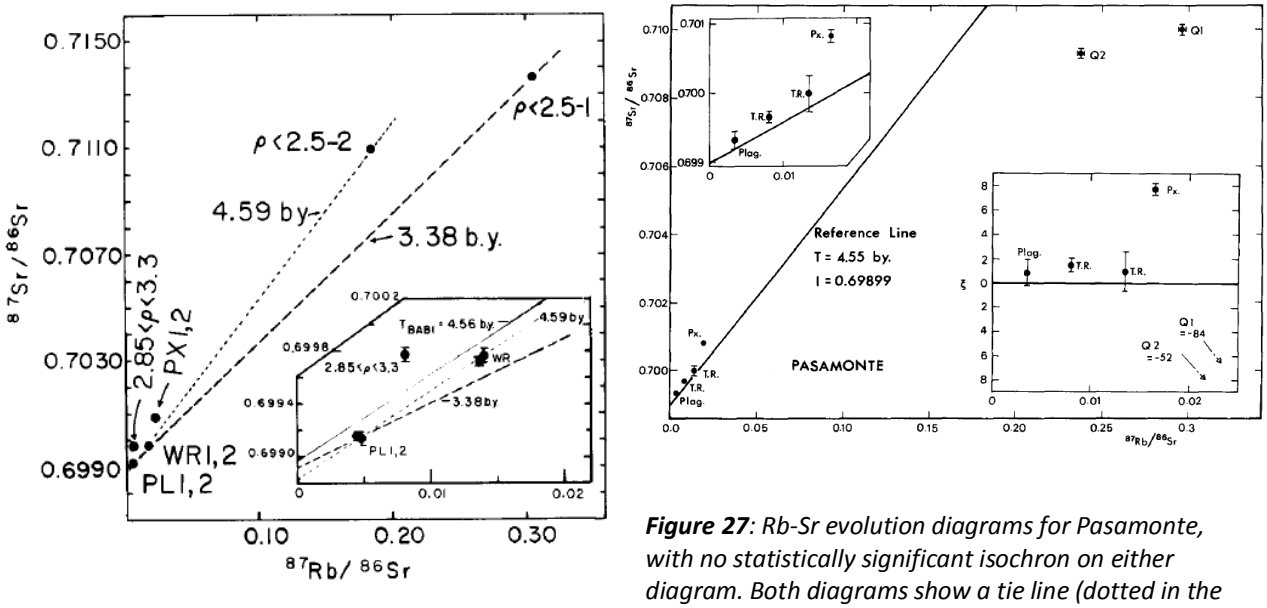


***Figure 27****: Rb-Sr evolution diagrams for Pasamonte, with no statistically significant isochron on either diagram. Both diagrams show a tie line (dotted in the diagram at left) connecting whole rock and plagioclase Rb-Sr values, giving an age of 4.55-4.59 Ga; while these ages do not represent actual events, they suggest that the system achieved isotopic closure early (~4.5-4.6 Ga) and experienced a severe disturbance later in its history, possibly 2.5-2.9 Ga (Birck and Allegre, 1978). This isotopic disturbance is also likely related to the event that liberated Pasamonte from its parent body (Unruh et al, 1977). Top diagram from Unruh et al (1977), bottom diagram from Birck and Allegre (1978).*

*K-Ar/Ar-Ar*. The first reported K-Ar ages for Pasamonte (3.80 ± 0.23 Ga: Geiss and Hess, 1958; 4.25 Ga: republished from the German literature in Anders, 1963) were significantly younger than other published Rb-Sr values, and suggested that one or both systems were disturbed. An average of early literature values (3.5 Ga: Heymann et al, 1968) showed a significant amount of scatter in the range of measured ages (2.9-3.9 Ga), though one older age (4.5 Ga) was reported by Rieder and Wanke (1969).

Podosek and Huneke (1973) analyzed K-Ar chronology in Pasamonte and found evidence of "partial diffusive loss" for argon; an intermediate plateau age of ~4.1 Ga that persisted for 70% of the cumulative argon release was interpreted as the age of major Ar loss, while a high-temperature age of 4.51 ± 0.04 Ga was taken as the lower limit for a crystallization age (Podosek and Huneke, 1973; **Figure 28**). Similar results were attained by Kunz et al (1992, 1995) in an analysis of three separate clasts from Pasamonte; low-temperature K-Ar ages of 3.9-4.1 Ga were inferred to represent brecciation and compaction events, while a concordant high-temperature K-Ar age of 4.4 ± 0.1 Ga was seen as a lower limit to the formation age of Pasamonte (**Figure 29**). The chondritic-contaminated granulitic breccia clast (analyzed in Metzler et al, 1995) showed an intermediate plateau age (lasting over 50% of Ar release) of 4.245 ± 0.024 Ga, and as this age probably represents the time of recrystallization and the formation of granulitic texture (Kunz et al, 1995), it may thus also signify the time this single clast was into the Pasamonte parent body regolith.

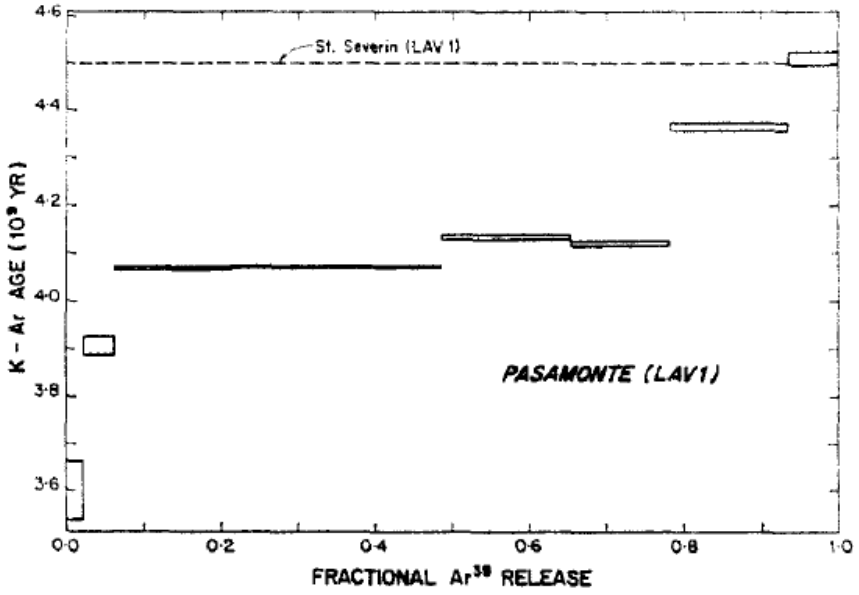


***Figure 28**: Apparent K-Ar ages as a function of fractional Ar release in Pasamonte. The apparent ages increase monotonically with increasing Ar release, suggesting diffusive loss of Ar. The intermediate plateau age of ~4.1 Ga is likely related to Ar loss around this time, and the highest temperature age (4.50 ± 0.04) is taken as the lower time limit for crystallization. From Podosek and Huneke (1973).*

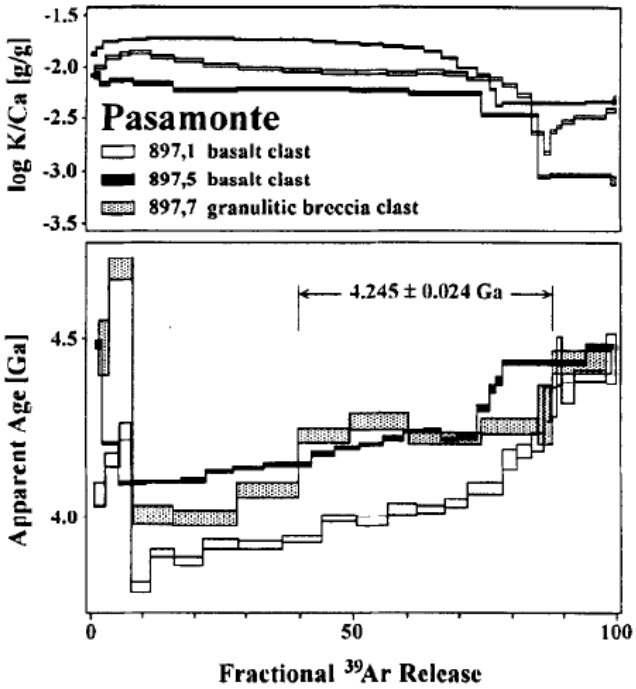


***Figure 29**: K/Ca ratios and apparent K-Ar ages from fractional Ar release. From Kunz et al (1995).*

A recent Ar-Ar study of Pasamonte, however, has indicated younger K-Ar ages than previously reported (average apparent age: 3.8 ± 0.2 Ga, high-T age: 3.9 ±0.09 Ga; Shankar et al, 2008, **Figure 30**), and thus more work is necessary to clarify the complex Ar-loss history of Pasamonte.

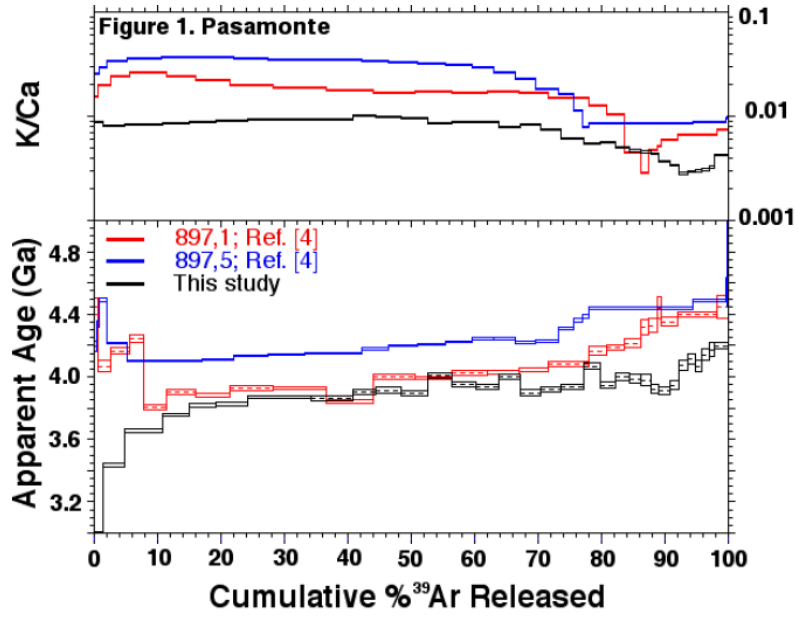


***Figure 30**: K/Ca ratios and apparent K-Ar ages as a function of Ar release. The blue and red data are taken from Kunz et al (1995), in **Figure O-R**, above. From Shankar et al (2008).*

*U-Th-Pb/Pb-Pb*. Manhes et al (1975) and Nakamura et al (1976) found that U-Pb data showed a Pb-excess discordancy on a U-Pb concordia diagram for Pasamonte; Nakamura et al (1976) determined a Pb-Pb internal isochron age of 4.57 ± 0.01 Ga, which was interpreted as the age of differentiation for the Pasamonte parent material. Unruh et al (1977) determined a similar Pb-Pb age from whole rock and mineral separates (4.53 ± 0.03 Ga; **Figure 31**); U-Pb data was found to be significantly discordant (**Figure 32**), but a U-Pb concordia plot (**Figure 33**) suggested possible ages of 4.45-4.57 Ga (indicating early formation at 4.57 Ga and later brecciation at or after 4.45 Ga), with a very recent (0-0.006 Ga) disturbance causing resetting during excavation on the parent body or entry into the earth's atmosphere. A more recent analysis of U-Pb, in Pasamonte zircons, found a similar concordant age of 4.56 Ga (Bukovanska and Ireland, 1993).

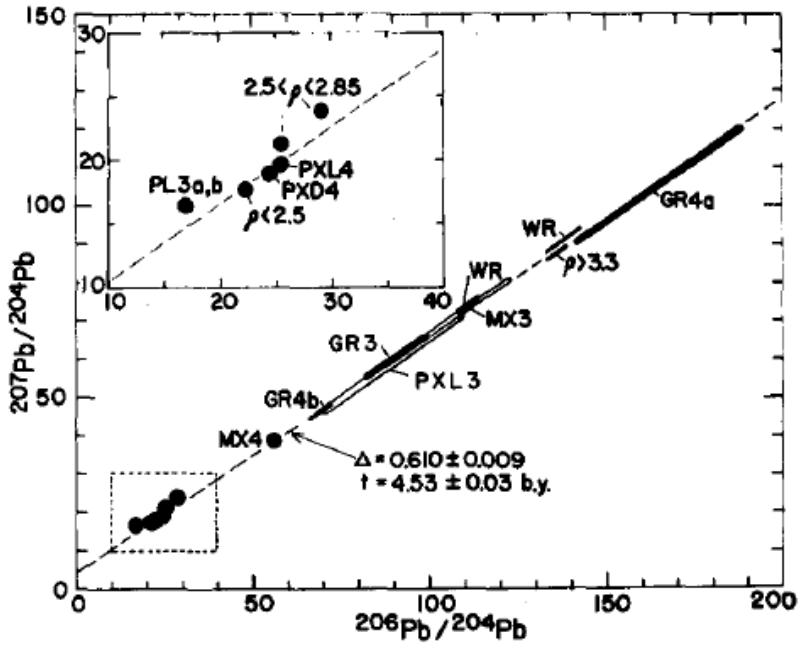


***Figure 31**: Pb-Pb diagram for mineral separates and whole-rock Pasamonte samples. The dotted line corresponds to an age of 4.53 ± 0.03 Ga. From Unruh et al (1977).*

*U-Th-$^4$He*. The range of U-Th-$^4$He ages reported in the literature spans from 1.4 Ga (Rieder and Wanke, 1969) to 3.6 Ga (Anders, 1963); Heymann et al (1968) reported a literature average of 2.4 Ga. These data indicate that Pasamonte has probably undergone He loss at some point in its history.

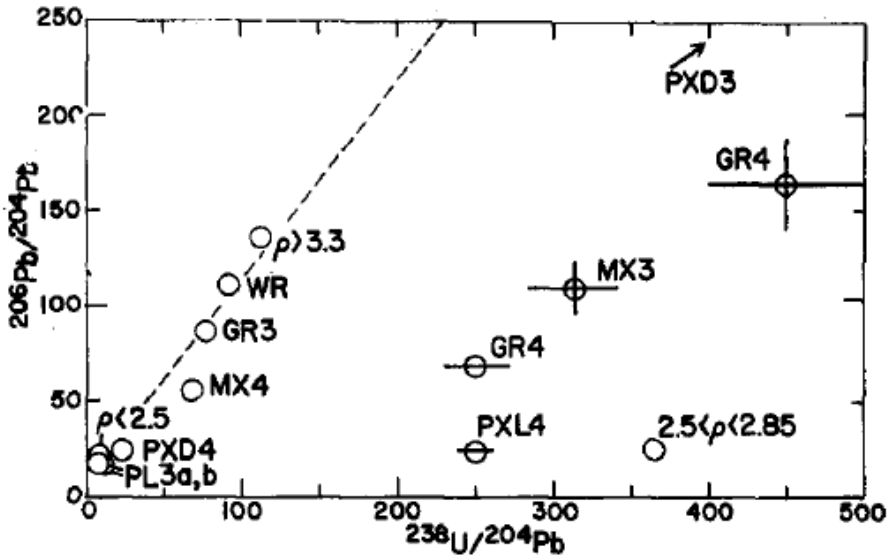


***Figure 32**: U-Pb/Pb-Pb parent-daughter evolution diagram for Pasamonte. The dashed line corresponds to an age of 4.56 Ga, but many samples from Pasamonte are notably discordant, including PXD3, which plots completely off the diagram. The cluster of points near the origin may be related to recent resetting on the parent body (i.e., the event that liberated the meteorite) or resetting during atmospheric entry. From Unruh et al (1977).*

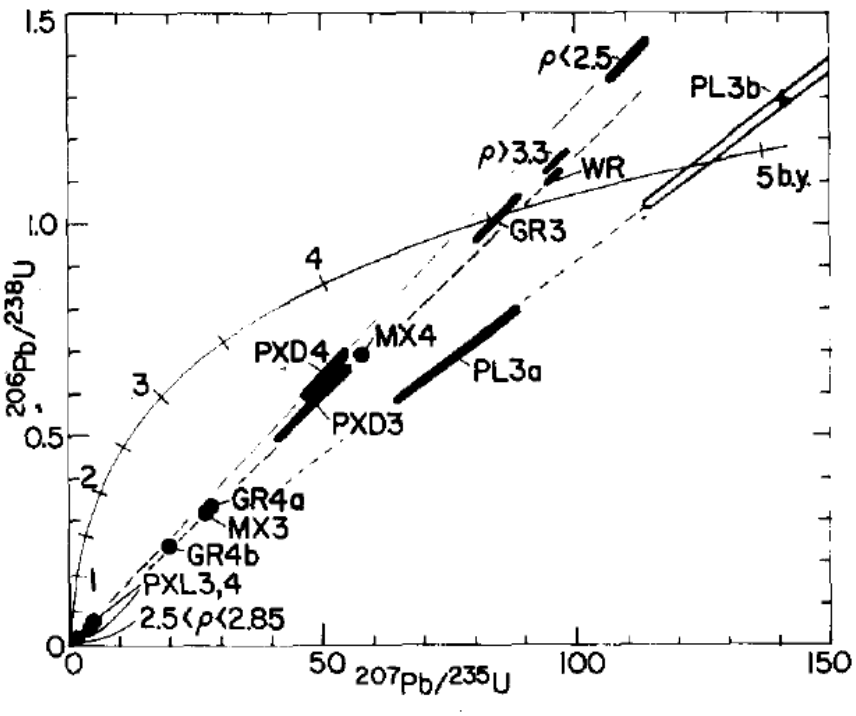


***Figure 33**: U-Pb concordia plot for both mineral separates and whole-rock Pasamonte samples. Most of the data (excluding PL3a, b) is defined by an envelope with points at 4.45 Ga, 4.57 Ga, and 0.006 Ga, while the PL3a and PL3b data define a tie line between ~0 and 4.9 Ga. Though these ages in themselves are unlikely to represent real events in the history of the meteorite, the interval 4.57-4.45 Ga could reflect approximate ages of formation and later brecciation; the lower intercept at ~0.006 Ga is probably related to the impact event that formed the meteorite (or atmospheric entry). From Unruh et al (1977).*

*Sm-Nd*. The first published Sm-Nd age-date for Pasamonte was put forth by Nakamura et al (1976), who defined an internal isochron age of 4.56 ± 0.14 Ga, based on both mineral separates and whole-rock samples; however, the pyroxene fraction, with higher Sm/Nd ratios, was found to be significantly

discordant from this isochron. Unruh et al (1977) published a revised, concordant Sm-Nd age of 4.58 ± 0.12 Ga (**Figure 34**); as the Sm-Nd shows no evidence of later metamorphic disturbances seen in other age-dating systems, it was interpreted as the age of formation for Pasamonte. However, Pasamonte is not concordant with the Sm-Nd whole-eucrite isochron, as are other eucrites with anomalous oxygen isotopes, suggesting the possible influence of chondritic contamination (Blichert-Toft et al, 2002) or derivation of Pasamonte from a unique parent body (e.g., Scott et al, 2009).

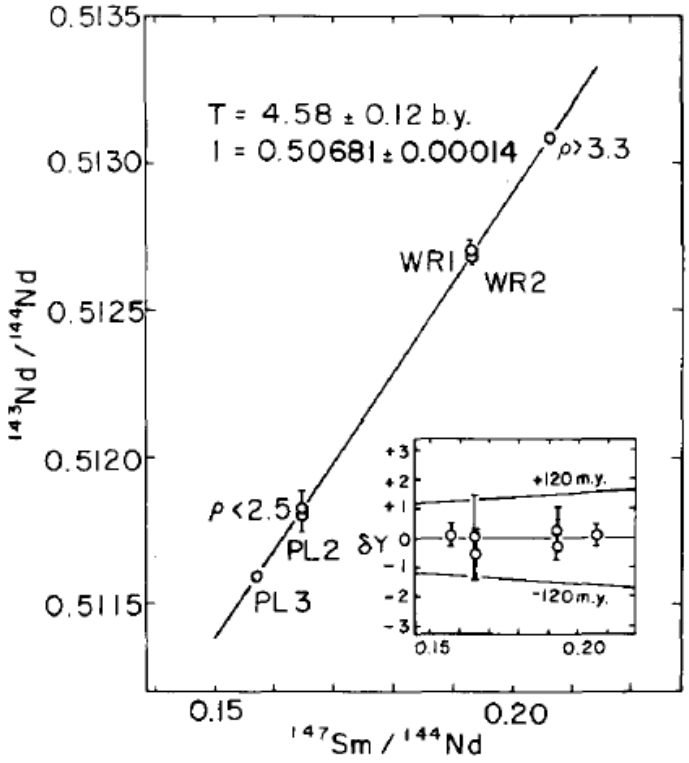


***Figure 34**: Sm-Nd evolution diagram for Pasamonte, with mineral separates and whole-rock values plotted on a single isochron, defining a formation age of 4.58 ± 0.12 Ga. From Unruh et al (1977).*

*Hf-W*. Pasamonte whole-rock samples were found to be concordant with a eucrite whole-rock Hf-W isochron corresponding to a eucrite formation age of 11.1 ± 1.1 Ma after chondrite formation (Quitte et al, 2000).

*Lu-Hf*. Pasamonte whole-rock samples were combined with other eucrite samples to define a whole-rock eucrite Lu-Hf isochron corresponding to an early formation age (4.604 ± 0.039 Ga), though this isochron is not statistically significant (MSWD = 4.52; Blichert-Toft et al, 2002). Other authors have investigated Lu-Hf systematics in Pasamonte (e.g., Patchett and Tatsumoto, 1980; Albarede et al, 2006) but these sources do not report ages based on their data.

*Pu-Xe*. Early Xe work on Pasamonte (e.g., Rowe and Kuroda, 1965; Rowe and Bogard, 1966; Hohenberg et al, 1967) revealed a significant excess of fissiogenic xenon that was inferred to be from a source other than uranium fission. These results were first presented by Rowe and Kuroda (1965), who found these anomalies in a single Pasamonte sample (**Figure 35**); these authors determined that the Xe excess was produced from the spontaneous fission decay of an extinct nuclide, e.g., $^{244}Pu$, and thus a Pu-Xe formation interval (representing the elapsed time between the end of galactic nucleosynthesis and the formation of the meteorite) of 300 Ma was calculated for Pasamonte. (Pepin, 1966 then recalculated

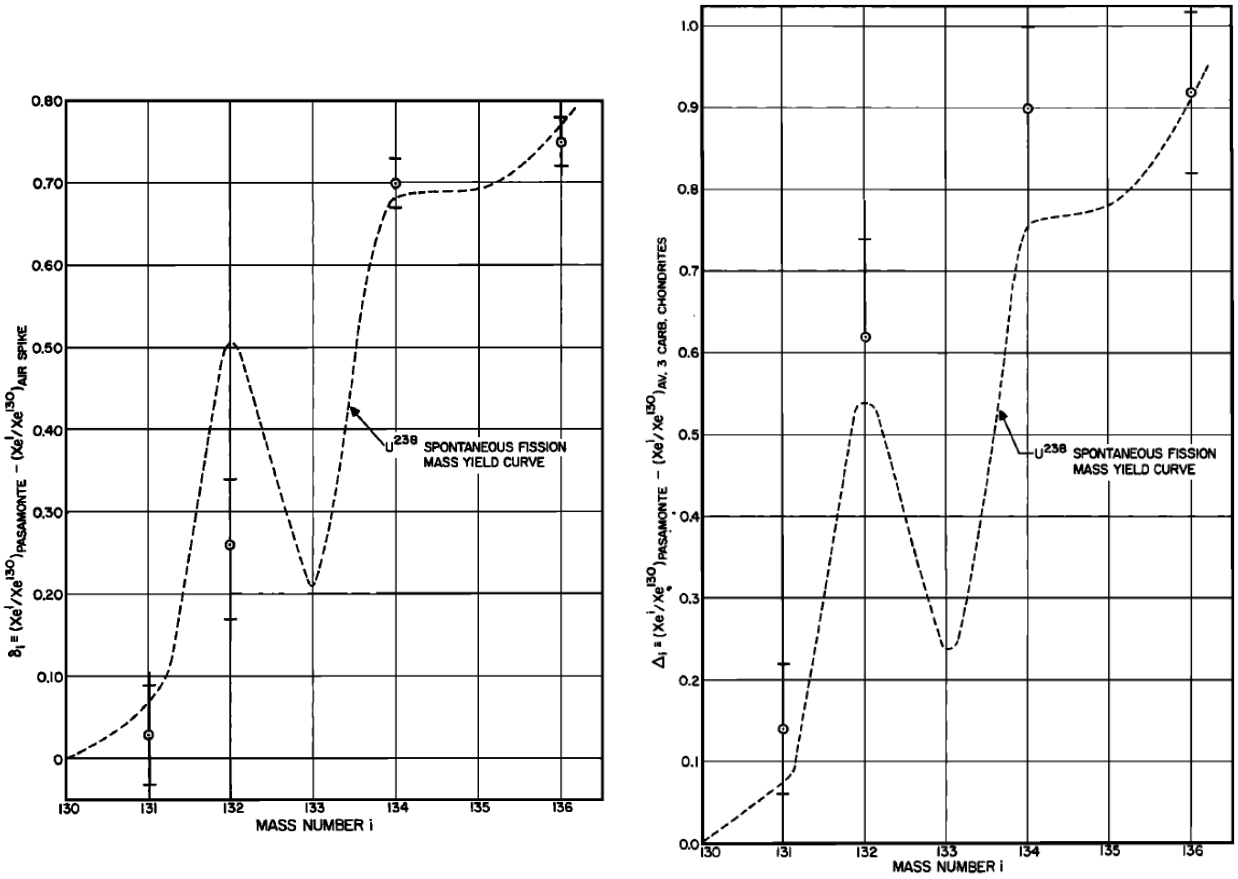


***Figure 35****: Excess fissiogenic xenon isotopes in a single Pasamonte sample (circles with error bars) relative to atmospheric concentrations (left) and carbonaceous chondrites (right). The $^{238}$U spontaneous fission mass yield curve is shown on both diagrams for comparison, and suggests that these xenon excesses in Pasamonte are from a source other than uranium fission. From Rowe and Kuroda (1965).*

this value to 220 Ma after subtracting out a small cosmogenic Xe component.) A second sample of Pasamonte, analyzed by Rowe and Bogard (1966), showed an even greater Xe isotopic anomaly (**Figure 36**), though the authors were careful to note that overall Xe abundances in Pasamonte were lower than in any other measured meteorite. Other contemporary studies reported various formation intervals for Pasamonte (Pu-$^{136}$Xe = 300 Ma, I-$^{129}$Xe = 300 Ma: Kuroda et al, 1966; U-$^{136}$Xe = 255 ± 40 Ma, I-$^{129}$Xe = 235-275 Ma: Rowe, 1967) as well as further constraints on the isotopic composition of xenon in the meteorite (e.g., Pepin, 1966; Eberhardt and Geiss, 1966; Rowe, 1967; Hohenberg et al, 1967).

Recent work has clarified Pu-Xe fission ages relative to the angrite Angra dos Reis (ADOR), with Pasamonte Pu-Xe ages (4.559 ± 0.025 Ga, 4.576 ± 0.019 Ga) appearing to be slightly older or contemporaneous with ADOR (Michel and Eugster, 1994; Shukolyukov and Begemann, 1996b). This is consistent with the unequilibrated nature of Pasamonte (Shukolyukov and Begemann, 1996b).

*Mg-Cr*. Whole-rock eucrite samples, including Pasamonte, were used to define a Mn-Cr whole-eucrite isochron of 4.5649 ± 0.0011 Ga (Trinquier et al, 2008). This isochron is parallel to, but significantly offset (-0.4$\varepsilon_{Cr}$) from the eucrite Mg-Cr isochron determined by Lugmair and Shukolyukov (1998), due to a revised initial estimate of $\varepsilon_{53Cr}$ (-0.12 ± 0.05).

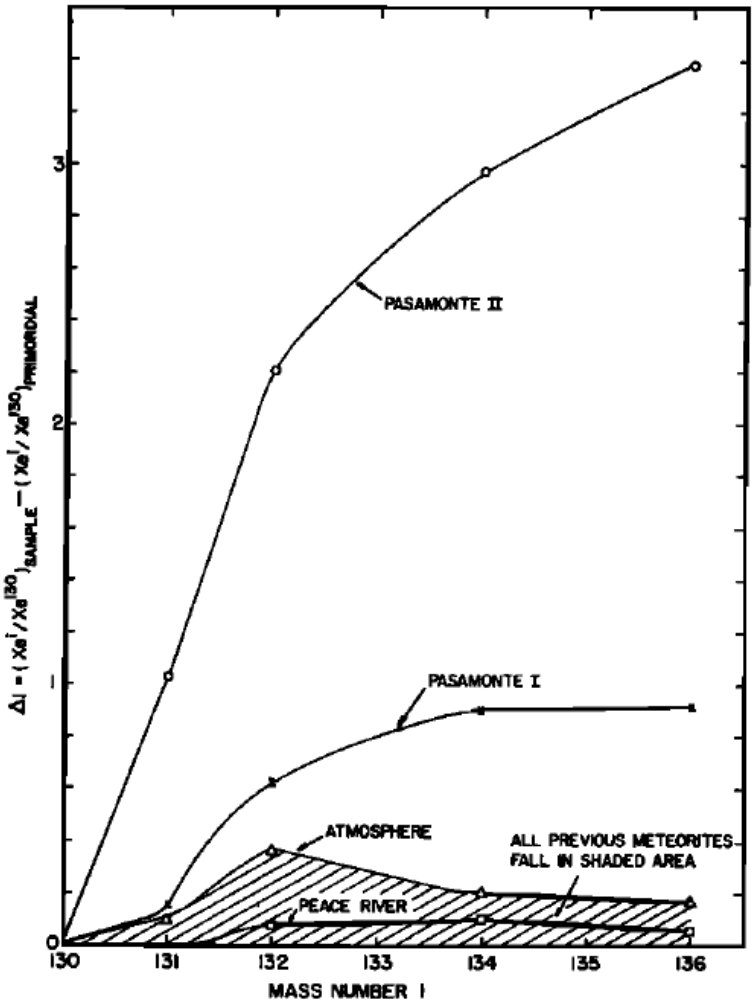


***Figure 36**: Xenon anomalies in Pasamonte I (Rowe and Kuroda, 1965) and Pasamonte II (Rowe and Bogard, 1966), relative to primordial isotopic Xe abundances. Other meteoritic Xe compositions from the literature at the time are plotted for comparison. From Rowe and Bogard (1966).*

*Summary*. Pasamonte formation and crystallization ages are generally concordant between different isotopic age dating system at ~4.5-4.6 Ga (Rb-Sr, Pb-Pb, Sm-Nd, Hf-W, Lu-Hf, Pu-Xe, and Mg-Cr ages), but the timing of various disturbances is much less clear, with possibilities at ≤100 Ma after formation (Pb-Pb: Unruh et al, 1977), at 3.9-4.1 Ga (K-Ar: Podoske and Hunuke, 1973; Kunz et al, 1992, 1995), at 2.5-2.9 Ga (Rb-Sr: Birck and Allegre, 1978), and probably very recently as well, associated with the liberation of the meteorite from its parent body or atmospheric entry (Rb-Sr, Pb-Pb: Unruh et al, 1977). For a comprehensive discussion relating Pb-Pb, Rb-Sr, and Sm-Nd ages, see Unruh et al (1977).

**Cosmogenic Isotopes and Cosmic-Ray Exposure Ages**

A summary of researchers and their cosmogenic noble gas exposure ages can be found in **Table 4**, below. Other isotopic information on the cosmogenic noble gases in Pasamonte can be found in Hohenberg et al (1967), Schultz and Kruse (1989), Eugster and Michel (1995), and Busemann and Eugster (2002).

**Table 4**: CRE ages for Pasamonte. (S&B refers to Shukolyukov and Begemann, see bibliography for full citation.)

| source | Eberhardt and Hess 59 *in* Goles et al 60 | Heymann et al 68 literature average | Podosek and Huneke 73 | Hudson 81 | Aylmer et al 88 | S & B 94 | S & B 96a | S & B 96b |
|---|---|---|---|---|---|---|---|---|
| **3He** | | 5.1 | | | | | | |
| **38Ar** | 9 | | 6 ± 2 | | 5.1 | | | |
| **81Kr** | | | | 8.2 ± 0.7 | | 7.2 ± 0.7 | 7.4 ± 0.5 | |
| **126Xe** | | | | | | | | 7.7 ± 0.4 |

**Other Isotopes**

*Oxygen.* Oxygen isotope systematics in Pasamonte were first investigated by Taylor et al (1965), who measured $\delta^{18}O$ in plagioclase (4.5‰ ± 0.2‰), pyroxene (4.1‰ ± 0.2‰), "free silica" (12.5‰), and a whole-rock sample (4.3‰); these values are within the range determined for other HED achondrites. Slightly lower $\delta^{18}O$ values were determined for Pasamonte by Clayton and Mayeda (1983, 1996) at 3.77‰; these studies also reported $\delta^{17}O$ (1.81‰), $\Delta^{17}O$ (-0.15‰), and $^{18}O$ excess (+0.31‰). The Clayton and Mayeda (1983, 1996) $\delta^{18}O$ and $\delta^{17}O$ values for Pasamonte are higher than all other HEDs measured in the studies, with the exception of Ibitira and ALH76005.

Recent studies (e.g., Wiechert et al, 2004; Greenwood et al, 2005; Scott et al, 2009) have confirmed the unusual oxygen isotopic signature in Pasamonte. Wiechert et al (2004) reported oxygen isotope values that were similar to those of Clayton and Mayeda (1983, 1996) ($\delta^{18}O$ = 3.694-3.744‰, $\delta^{17}O$ = 1.769-1.809‰, and $\Delta^{17}O$ = -0.191‰ ± 0.015‰, -0.177 ± 0.017); these values are consistent with $^{16}O$ depletion, giving Pasamonte a less negative $\Delta^{17}O$ value than . In a discussion of possible causes for this anomalous isotopic composition, Wiechert et al (2004) ruled out weathering effects (which would significantly shift $\delta^{18}O$ values), a distinct parent body separate from other HEDs (because of similar chemistry between Pasamonte and other HEDs), and contamination with admixed chondritic material (which would result in higher-than-observed Ni and Ir values), ultimately suggesting that Pasamonte and other anomalous eucrites may have tapped a heterogeneous oxygen isotope reservoir on the eucrite parent body.

Similar oxygen isotopic values were put forth by Greenwood et al (2005) ($\delta^{18}O$ = 3.784‰ ± 0.105‰, $\delta^{17}O$ = 1.779‰ ± 0.049‰, and $\Delta^{17}O$ = -0.205‰ ± 0.012‰) and Scott et al (2009) ($\delta^{18}O$ = 3.823‰ ± 0.100‰, $\delta^{17}O$ = 1.800‰ ± 0.052‰, and $\Delta^{17}O$ = -0.204‰ ± 0.008‰). Greenwood et al (2005) inferred that these isotopic compositions could be the result of 3-3.5% mixing with a chondritic (H or CI) component, citing the clearly chondritic-influenced granulite breccia clast in Pasamonte reported by Metzler et al (1994, 1995). However, the oxygen isotope values from Scott et al (2009) were determined from three unique Pasamonte samples (a black clast, light matrix, and third "uncharacterized" sample); the $\Delta^{17}O$ values from these samples were indistinguishable, and thus the oxygen isotope character in Pasamonte must have been derived from a single, isotopically homogenous source (Scott et al, 2009). This source was probably not an isotopically heterogeneous HED parent body as suggested by Wiechert et al (2004), as no other unmetamorphosed eucrites (and polymict eucrites with unmetamorphosed clasts) produce aberrant $\Delta^{17}O$ values (Scott et al, 2009). This leaves the most plausible explanation for Pasamonte's oxygen isotope composition as a separate parent body from the other HEDs (Scott et al, 2009).

*Carbon.* Carbon isotope systematics were investigated in Pasamonte by Grady et al (1997), who found $\delta^{13}C$ = -23 for total Pasamonte carbon (i.e., including terrestrial contamination); this isotopic composition is the same for carbon evolved at >600°C (i.e., free from terrestrial contamination).

*Beryllium.* Literature values of $^{10}Be$ content in HEDs were summarized by Aylmer et al (1988), who reported a Pasamonte $^{10}Be$ content of 22.3 ± 2.6 dpm/kg.

*Boron.* $^{11}B/^{10}B$ was reported as 3.960 ± 0.008 for Pasamonte by Shima (1963); Bassett (1990) used this value to calculate a $\delta^{11}B$ of -21‰ ± 2.0‰.

*Lithium.* Pasamonte has been included in a number of recent lithium analyses in achondrites (e.g., Herd et al, 2004; Magna et al, 2006; Beck et al, 2006; Bell et al, 2008; Rieck et al, 2008). Magna et al (2006) reported a whole-rock $\delta^7Li$ value of 3.65‰ ± 0.20‰; Rieck et al (2008) reported on lithium isotope variation in different minerals from Pasamonte, finding little evidence of preserved isotope zoning, with pyroxene crystals ranging in $\delta^7Li$ from -4‰ to +10‰ and isotopically lighter plagioclase varying in $\delta^7Li$ from -15‰ to -5‰ (**Figure 37**).

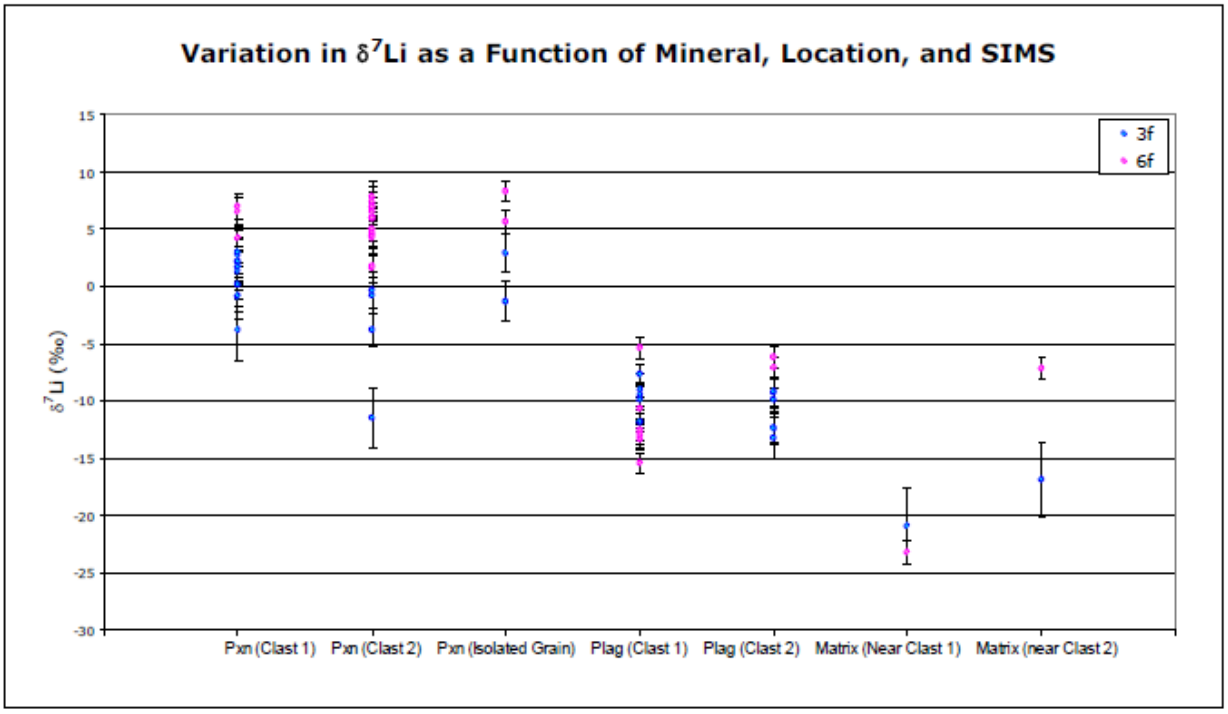


***Figure 37**: $\delta^7Li$ for Pasamonte minerals, with pyroxene showing heavier Li isotopic composition than plagioclase. From Rieck et al (2008).*

*Iron.* Iron isotopes were analyzed in a variety of planetary materials by Poitrasson et al (2004). Pasamonte values ($\delta^{57}Fe/^{54}Fe$ = 0.066‰ ± 0.093‰, $\delta^{57}Fe/^{56}Fe$ = 0.018‰ ± 0.237‰) are higher than many other HED samples, but are similar to the mean HED data (within error); they are also very similar to Martian (SNC) meteorites, but lighter than terrestrial or lunar samples, suggesting different processes of planetary formation. Schoenberg and von Blanckenburg (2006) reported values for $\delta^{56}Fe$ (-0.013‰ ± 0.046‰), $\delta^{57}Fe$ (0.007‰ ± 0.073‰), and $\delta^{58}Fe$ (0.02‰ ± 0.041‰) for Pasamonte that were indistinguishable from both SNC meteorites as well as chondrites.

*Magnesium.* Magnesium isotopic composition in Pasamonte was first investigated by Hsu and Crozaz (1996) in an attempt to quantify the decay of primordial $^{26}Al$; $\delta^{26}Mg$ values ranged from -2.7‰ ± 2.8 to 7.2‰ ± 3.7‰, which are similar to terrestrial compositions (within error), and thus no evidence was found for the past presence of live $^{26}Al$ in Pasamonte. Other measured Pasamonte Mg isotope values ($\delta^{26}Mg_{DSM3}$ = -0.13‰ ± 0.02‰, $\delta^{26}Mg_{DSM3}$ = -0.07‰ ± 0.01‰, $\Delta^{25}Mg$ = -0.008‰ ± 0.015‰; Wiechert and Halliday, 2007) are very similar to other HEDs, terrestrial samples, lunar, Martian, and chondritic values; all measured values plot on a common fractionation curve, suggesting a single homogenous Mg reservoir for the solar system.

*Aluminum.* Early reported $^{26}Al$ contents in Pasamonte include 99 ± 11 dpm/kg (originally published in Rowe et al, 1963; corrected by Rowe and Clark, 1971) and 101.5 ± 3.8 dpm/kg (Fuse and Anders, 1969); Aylmer et al (1988) summarized a number of other literature values with a slightly lower average (~94 dpm/kg).

*Calcium.* Backus et al (1964) reported a $^{40}Ca/^{44}Ca$ ratio of 43.67 for Pasamonte; this is much lower than a more recently calculated value of 47.129 ± 0.004, which was found to be slightly lower (≤0.02) than other HEDs, SNCs, and lunar rocks (Shih et al, 1993).

*Other.* Rare earth element (REE) isotopic ratios were reported for Ce ($^{140}Ce/^{142}Ce$ = 8.3±0.2), Yb ($^{169}Yb/^{174}Yb$ = 0.0043 ± 0.002), and Lu ($^{175}Lu/^{176}Lu$ = 40.2 ± 1.4) by Schmitt et al (1963); these values are not significantly different than those measured on terrestrial samples. $^{138}Ce/^{142}Ce$ (0.0228518 ± 0.0000026) was reported by Shimizu et al (1984), though this value was later corrected by Makishima and Masuda (1993) to 0.0225647 ± 0.0000026 based on new correction factors.

Zr isotopic ratios in Pasamonte were first investigated by Minster and Allegre (1982), who published values for $^{91}Zr/^{90}Zr$ (0.5 ± 1.4), $^{92}Zr/^{90}Zr$ (0.0 ± 1.5), and $^{96}Zr/^{90}Zr$ (5.5 ± 3.7), which were interpreted as non-anomalous compositions (i.e., similar to other planetary materials). Schonbachler et al (2003) reported $\varepsilon^{91}Zr$ (0.0 ± 0.6), $\varepsilon^{92}Zr$ (0.0 ± 0.4), and $\varepsilon^{96}Zr$ (0.3 ± 1.5) for Pasamonte; these values are consistent with other meteorites and lunar samples, as well as CAIs (excluding $\varepsilon^{96}Zr$, which is slightly higher for CAIs).

**Experiments**: Chapman and Salisbury (1973) analyzed the reflectance spectra of a number of different meteorites, finding that Pasamonte had similar features to 4 Vesta but an exaggerated color and absorption band (**Figure 38**). Nuclear track experiments by Wilkening and Parker (1977) revealed much higher track densities in the clasts than the host, but no fission track plateaus were identified; however, track densities suggested atmospheric ablation on the order of 2-3 cm.

Cathodoluminescence techniques have revealed zoned plagioclase and two different populations of silica in Pasamonte (discussed above in the section on mineral chemistry) (Batchelor, 1991). Pasamonte has also been analyzed by thermoluminescence (Sears et al, 1991; Batchelor and Sears, 1991), from which a perihelion of 0.5-0.8 AU was calculated by Benoit et al (1991). Recent investigations of magnetic anisotropy revealed a slightly weaker magnetic fabric for Pasamonte relative to other eucrites (Gattacceca et al, 2008).

The petrogenesis of the Pasamonte eucrite has been investigated by a number of workers. According to the Consolmagno and Drake (1977) model, a 10% equilibrium melt of a source region composed of 50% olivine, 30% metal, 10% orthopyroxene, 5% clinopyroxene, and 5% plagioclase could reproduce

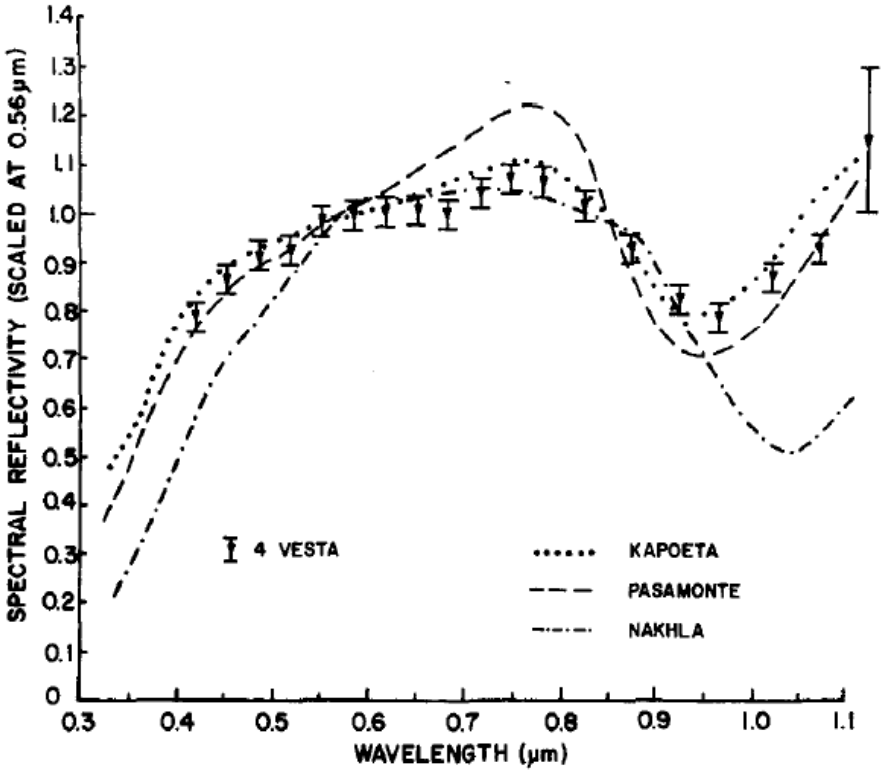


***Figure 38**: Reflectivity curves for Kapoeta, Pasamonte, and Nakhla, relative to asteroid 4 Vesta; Pasamonte shows similar features, but they are slightly exaggerated in the meteorite. From Chapman and Salisbury (1973).*

Pasamonte-like major and trace element concentrations. Stolper (1977) contended that Pasamonte could have been created by a 10-20% differentiation of a Sioux County-like liquid, which in turn would have been created by a 15-20% partial melt of slightly different source region (olivine, pyroxene, plagioclase, Cr-rich spinel, and metal). Trace element modeling calculations confirmed that Pasamonte could be derived from a differentiated Sioux County-like liquid by plagioclase and pigeonite fractional crystallization (Ma et al, 1977; Fukuoka et al, 1977), though lower trace-element abundances in Pasamonte indicate that the source was not strictly related to Sioux County (Hsu and Crozaz, 1996). REE analyses similarly indicate that *both* fractional crystallization and partial melting of a chondritic source could produce Pasamonte-like REE patterns (Shimizu and Masuda, 1986).

**Metamorphism**: Early petrographic and chemical investigations of Pasamonte revealed preserved igneous zoning in both plagioclase and pyroxene (Duke and Silver, 1967), wide ranges in pyroxene Mg#, departures from stoichiometry in plagioclase, and abundant fine-grained mesostasis in lithic clasts (Reid and Barnard, 1979; BVSP, 1981). These clues suggested that Pasamonte was unequilibrated relative to the more homogenous, equilibrated compositions of the main-group eucrites (Reid and Barnard, 1979), and these features were probably preserved by initially rapid cooling, i.e., a high degree of supercooling (Reid and Barnard, 1979; Delaney et al, 1982a; O'Neill and Delaney, 1982).

Further petrographic studies revealed clouding by exsolution in larger Pasamonte plagioclase grains but not in pyroxene (Harlow and Klimentidis, 1980); as this is an indication of the degree of homogenization of the meteorite (Takeda et al, 1983), it implied that Pasamonte did experience metamorphic conditions in its history, but at a lower temperature or for a shorter duration than other eucrites (Harlow and Klimentidis, 1980). Numerous other observations have supported this conclusion, including reports of minor post-brecciation annealing (BVSP, 1981; Takeda et al, 1983), low TL sensitivities (Batchelor and

Sears, 1991), subsolidus redistribution of certain elements (especially REE) without recrystallization (Phinney et al, 1993), impact-melt breccias and impact-formed glassy clasts (Metzler et al, 1994; 1995; Hsu and Crozaz, 1996), and pyroxene compositions indicative of slight metamorphism, relative to more unequilibrated clasts in polymict eucrites from Antarctica (Takeda and Graham, 1991). Age-dating relationships (Podoske and Hunuke, 1973; Unruh et al, 1977; Birck and Allegre, 1978; Kunz et al, 1992, 1995) also revealed a history of disturbances in certain isotopic systems, likely under metamorphic conditions, as would be necessary to violate closure temperatures for certain systems.

Miyamoto et al (1985) calculated possible thermal histories for Pasamonte pyroxenes; they determined that burial at >200 meters would result in homogenization, and Pasamonte was most probably buried at depths of less than 50 meters for most of its history, assuming either rock-like or regolith-like thermal diffusivities. A possible metamorphic history published by Metzler et al (1995) suggests initially rapid cooling (0.1-100$^{o}$C/hr: Walker et al, 1978) followed by brecciation and thermal metamorphism, with a second brecciation event at some later point. Textural evidence of late lamellar coarsening supports the contention that Pasamonte was unmetamorphosed prior to initial brecciation (Schwartz and McCallum, 2005), and complex Type 3 and Type 4 zoning patterns indicate that metamorphism (in this case metasomatism) occurred in the presence of a dry, Fe-rich, homogenous vapor phase (Schwartz and McCallum, 2005).

Recent research has focused on the apparent two-stage cooling history experienced by Pasamonte pyroxenes. Brearley et al (1993) noted that initially rapid cooling would preserve thinner, shorter-wavelength exsolution features in pyroxene cores, while later slow cooling would produce thicker and higher-wavelength exsolution lamellae in the rims, as well as lamellar coarsening in Fe-rich grains (Schwartz and McCallum, 2005). Similar results were obtained in a comprehensive analysis of pyroxene textures by Schwartz and McCallum (2005); cooling rates of 0.01$^{o}$C/day are necessary to produce the observed exsolution lamellae wavelength and thickness in pyroxene (**Figure 39**), and similar cooling rates were determined for the Fe-vapor cryptic metasomatism as observed in Type 3 and 4 zoning, again suggesting initially rapid basaltic cooling followed by a second thermal event with cooling rates that are 2-3 orders of magnitude slower. This cooling history implies initial basaltic flow thickness of ~20 meters with a cooling rate of 2.4$^{o}$C/day, followed by brecciation, mixing, and reburial at 2.5 meters, with a variable but significantly slower cooling rate (Schwartz and McCallum, 2005; **Figure 40**).

**Shock Effects**: Shock textures are almost absent from the Pasamonte eucrite; there is some variable fracturing in separated lithic clasts, but plagioclase grains from these clasts show uniform extinction and thus shock strain must have been <5 GPa (Kunz et al, 1995).

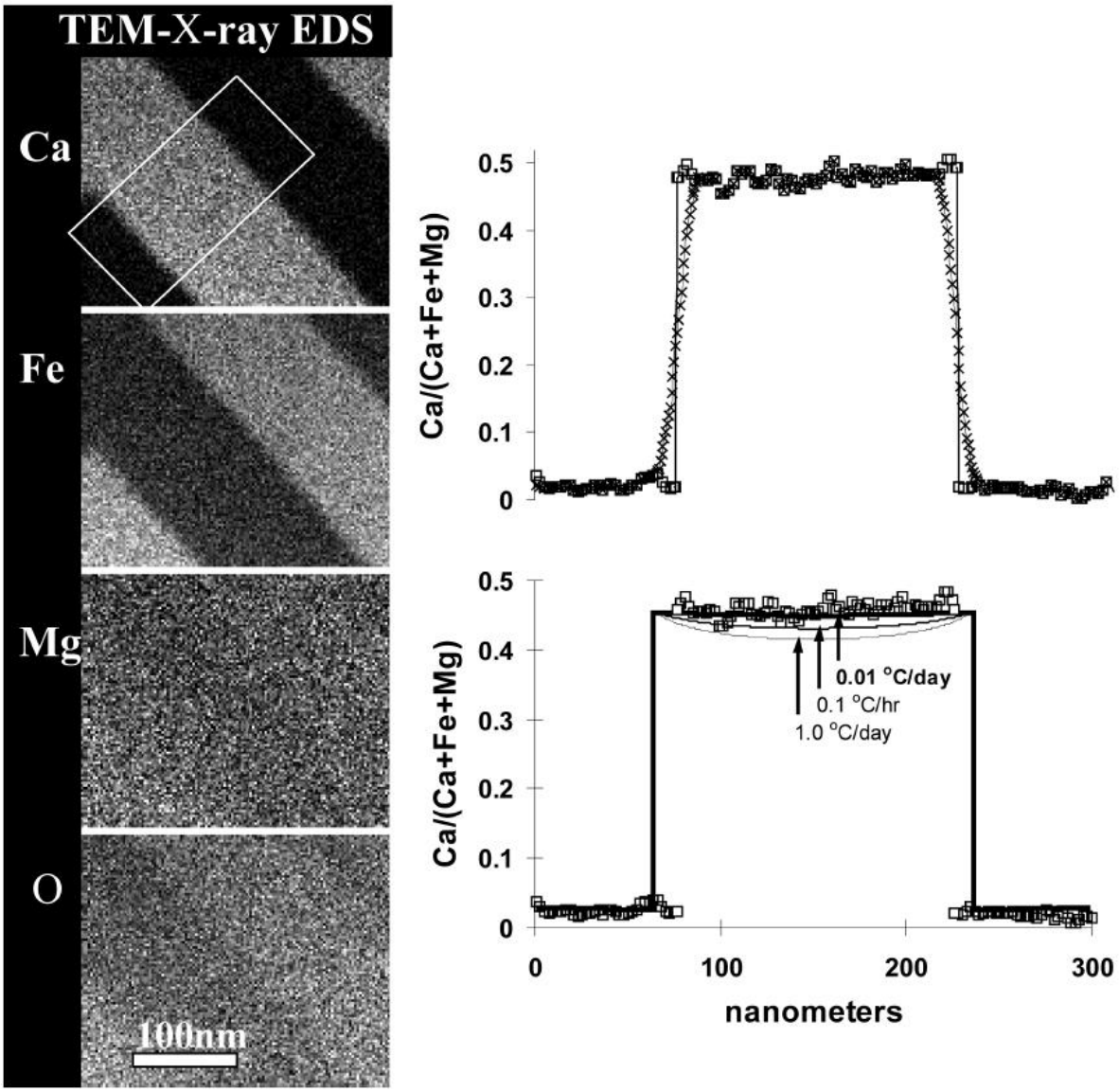


***Figure 39**: Left: TEM x-ray map of augite lamellae in a pigeonite host. Top right: EDX-TEM compositional profile (crosses), with deconvolved points as open squares. Bottom right: three cooling rates as modeled to produce the observed textures, with 0.01°C/day as the best fit. From Schwartz and McCallum (2005).*

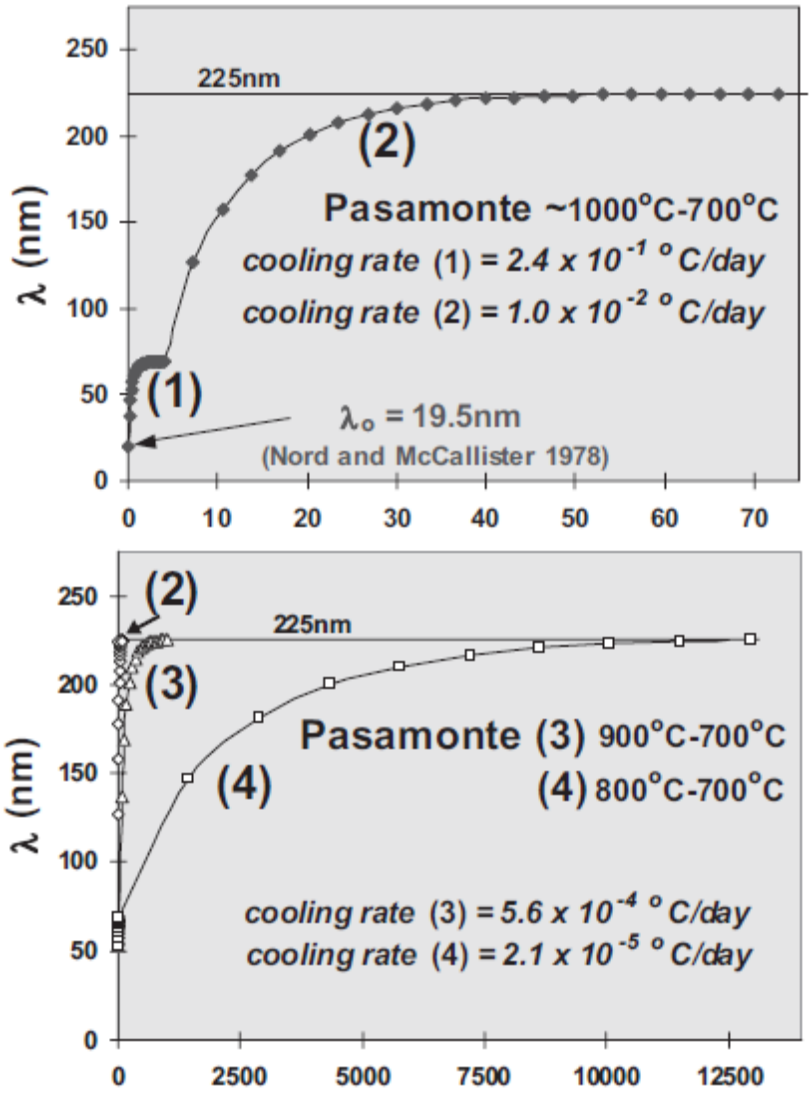


***Figure 40**: Calculated cooling rates based on lamellar wavelengths in Pasamonte pyroxenes. (1) refers to initial igneous cooling, while (2), (3), and (4) are cooling as a function of peak metamorphic temperature. From Schwartz and McCallum (2005).*